

Ladle furnace slag as a partial replacement of Portland cement

Paulo Sebastian Araos Henriquez^{a*}, Diego Fernando Aponte Hernandez ^a, Jordi Ibáñez Insa^b, Marilda Barra Bizinotto^a

^a Department of Civil and Environmental Engineering, Universitat Politècnica de Catalunya (UPC-BarcelonaTech), 08034 Barcelona, Spain.

^b Geosciences Barcelona (GEO3BCN), Spanish Council of Scientific Research (CSIC), 08028 Barcelona, Spain.

* Corresponding author. Department of Civil and Environmental Engineering, Universitat Politècnica de Catalunya (UPC-BarcelonaTech), Jordi Girona 1-3, 08034 Barcelona, Spain. E-mail address: paulo.sebastian.araos@upc.edu

Abstract: Ladle furnace slag (LFS) has been proposed as partial cement replacement due to its similar chemical composition with Portland cement. However, its mineralogical composition needs to be considered due to problems with expansive reactions and lower cementing activity. The objective of this study is to investigate the effect of particle size and mineralogical composition of LFS in cement-slag systems. The obtained results show a correlation between microstructural changes and macroscopic properties, lower mechanical performance and volumetric instability problems, although within the established limits in normal curing conditions. Therefore, it is concluded that LFS presents an interesting potential as cement replacement.

Keywords: Portland cement, ladle furnace slag, compressive strength, volume instability, microstructural characterization.

Highlights:

- LFS particle size and accelerated curing has an effect on volumetric instability.
- LFS-cement systems hydration proceeds similarly to ordinary Portland cement.
- In absence of free CaO the phase that leads to instability problems is free MgO.
- Partial cement replacement by LFS (25wt%) has limited mechanical negative effects.
- Physical-mechanical-microstructural properties were analyzed in LFS-cement systems.

1 Introduction

Portland cement industry is an important source of raw material consumption and greenhouse gas emissions to the atmosphere. It is estimated that cement production is responsible for approximately 6-7% of total CO₂ emissions [1] due to the intensive consumption of natural resources, the use of fossil fuels, and the intrinsic decarbonation process during cement production [2]. To reduce these negative externalities, the industry has introduced multiple improvements: a modernization and optimization of its industrial process in the last few years, the use of alternative fuels, the partial replacement of clinker in the cement production process with other materials such as residues for other industrial processes for their recovery, and the partial replacement of clinker to produce blended types of cement [1,3-5].

The steel industry has a significant increase in its production and will continue growing for the next 30 years according to recent studies [6,7]. The world steel association estimated that approximately 1808.6 million tons of crude steel was produced worldwide in 2018. Only in Spain, 14.3 million tons were produced in 2018 [8]. Steel production generates large amounts of residues, one of which is steelmaking slag. This waste is estimated to account for 15-20wt% of the total output [9]. These residues are dependent on the type of manufacturing process (melting or refining), type of furnace (basic oxygen furnace (BOF), electric arc furnace (EAF), ladle furnace (LF)), and the type of raw materials used in the manufacturing process (pig iron, recycled scrap). Accordingly, they can be classified as BOF slag (BOFS), EAF slag (EAFS), and LF slag (LFS) [10,11]. It is well known that

for every ton of EAF steel production, around 110 to 150 kg of EAFS and 20 to 30 kg of LFS are generated [12]. Nowadays, the steelmaking process of choice varies among different steel producers for many reasons, although future trends seem to favor the EAF / LFS production route due to a lower energy consumption and the possibility of reusing steel scrap. However, this method still generates a significant amount of waste [6,7]. For example, in the year 2018 in Spain, because its preferred steelmaking technologies are EAFS and LFS, an average of 0.43 million tons of LFS were generated [13].

LFS produced in the steelmaking process is an interesting waste to reuse, due to its physical properties, chemical composition similar to certain types of cement [14], affinity with cement-based materials, and high abundance as mentioned before. LFS naturally presents a granular dusty appearance with an average particle size distribution of 40–70% passing a 200-mesh sieve, with a maximum size of 2 mm [15-17]. Its density varies between 2.6-2.8 kg/m³ [16,18-20], with an specific surface area (SSA) around 2064-3091 cm²/g [15,21-24]. Its chemical and mineralogical composition varies due to many factors of the refining process, even within the same plant [25-28]. More than 60% of its weight is composed of calcium and silicon oxides. The other large group of compounds found in LFS corresponds to magnesium and aluminum oxides, which represent approximately just under 40% of total weight composition [17,25,29,30]. To a lesser extent iron, manganese, and titanium oxides can be found along with calcium sulfides and fluorides. Some LFS also may contain traces of heavy metals with a total content below 1%, such as chromium, zinc, or lead. Table 1-1 shows the average chemical composition present in LFS [23,37,38].

Table 1-1. Ranges values in the literature of chemical composition for LFS [19,28,37-40].

	CaO	SiO ₂	Al ₂ O ₃	FeO	Fe ₂ O ₃	MgO	SO ₃
Composition [%]	30-62	2-50	1-37	0-8	0-11	1-17	0-3

Regarding the mineralogical composition, this type of slag is characterized by the presence of phases with cementing or low/non-reactive activity typically from calcium-silicate and calcium-aluminate families. In addition, free CaO (lime) and free MgO (periclase), which are well known to cause problems of volumetric instability, are usually present in LFS. According to the literature, free CaO may [9,31-33] or may not be present [17,27,34-36] in LFS, as it may be consumed as a result of LFS weathering and/or maturity treatments. Instead, the presence of free MgO in LFS is more consistently reported in the technical literature, possibly due to a lower sensitivity to the previously mentioned treatments.

Some proposed applications for LFS in the construction industry include the production of steel and cement as a substitute for raw materials [10], as a base/sub-base material for pavements and road construction [15,41], soil stabilization [14,42], replacement of natural aggregates/filler in concrete products [43,44], and as a useful/cementitious material in mortars and concretes [35,37,45]. However, due to its high production volume and technological barriers in its valorization process, deposition in landfills is still the principal final destination of LFS. Other applications may be for agricultural and environmental purposes [46,47], soil amendment [48], heavy metal fixation [49,50], and even water depuration [51].

The main technological barriers in the use of LFS as a cement replacement are due to its volumetric instability and low cementing power/hydraulic activity problems. This mostly occurs due to the presence of certain unwanted phases formed in the refining steelmaking process, which are finally part of its mineralogical composition. Lime and periclase phases present in the LFS, if not treated previously, are the main responsible for expansion problems when hydrated/carbonated in cement-based matrices [17,28,40,52]. Also, reactive aluminum-silicates phases during hydration undergo a series of metastable phase transformations with different volume changes [53], or delayed hydration that can contribute to instability problems and low strength if gypsum is still available [54].

So far, only a few works have thoroughly investigated LFS as cement replacement in cement paste and mortars, mainly focusing in physical-mechanical performance, without considering the evaluation of its volume instability. Papayianni et. al. 2012 [31] studied the effects of granulometry in the cementitious properties of LFS-cement mortars. These authors used a 20wt% cement replacement with three different types of LFS and obtained good mechanical performance (between 75-95% of the control sample) depending on its granulometry, amorphous phases content and type of LFS lowering particle size treatment. More recently, Wang et. al. 2019 [54] have evaluated the feasibility of using LFS as a mineral addition in cement-based materials. These authors studied the initial reactions and mechanical performance of cement paste samples employing a 20wt% cement replacement and obtained poor mechanical performance (below 40% of the control sample). They concluded that it is not advisable to use the LFS in its natural state as a mineral addition, because LFS shows no pozzolanic and low cementing activity. These mostly associated to its high content of calcium-aluminates phases, affecting the normal hydration kinetics of cement, and not participating in the long term strength gain. In contrast, they proposed that it may present additional problems of instability when hydrating at latter ages. These differences in mechanical performance are associated to the variability of LFS mineralogical composition between different plants/sources. In turn, Herrero et. al. 2016 [35] investigated the hydration process of LFS, concluding that, in the presence of water, LFS exhibits an expansive process associated to the hydration of lime and periclase. Also, when used as a partial cement replacement in mortars (10-20 wt%), it was found that the chemical and mineralogical composition of the LFS affects the microstructure of the "cement-slag" system, with high-Al LFS showing better (mechanical and durability) performance than high-Si LFS. These authors found that both types of LFS exhibit an acceptable behavior of mechanical performance (in the range of concentrations studied), and also considered the evaluation of volume stability, thus concluding that an increase in the incorporated concentration could present instability problems associated with the free CaO and free MgO phases present in the slags. To solve these problems associated to the use of LFS as a cement replacement in general, three types of methods have been proposed: an accelerated weathering of LFS with different hydration process [35], a stabilization system subjecting the material to a carbonation process [55-57], and an air rapid cooling process (air quenching treatment) [32,33] in addition to a long weathering process. In spite of the potential use of LFS as a cement replacement, much research work remains to be carried out in order to assess its physical-mechanical properties, overall performance, and volume instability issues, which are not yet completely resolved due to the vast chemical and mineralogical variability of LFS.

The main objective of the present work is to study LFS-cement system to evaluate alternatives of partial cement replacement incorporating waste from other industries. Furthermore, the evolution of the microstructure and its correlation with physical-mechanical properties at the macroscopic level are investigated, with the aim of identifying possible changes in its performance. In particular, the impact of particle size and mineralogy of the LFS on the mechanical performance and volume instability of LFS-cement paste samples, with special interest in the free CaO and free MgO content. The purpose of these investigations is to reduce the tremendous environmental impact during the manufacturing process of Portland cement and the final disposal of LFS, a residue from the steel industry.

2 Materials and methods

2.1 Materials

The materials used in this study were commercially available cement type I 52.5 R, according to UNE-EN 197-1 [58], corresponding to a typical Portland cement composed mostly of clinker and minor phases such as gypsum and limestone, here labeled as CEM. Two types of ladle furnace slag from a Spanish steelmaking company were used, both from the same plant, but from different batches. The first one had a particle size distribution between 0-2 mm and was sieved directly on

site, with a calculated density of 2.82 g/cm^3 , according to UNE 80103:2013 [59], here labeled as LFS-G. The second type of LFS had all particles below 0.125 mm . This sample was sieved on-site to a size distribution between $0\text{-}2 \text{ mm}$ and milled in a ball mill to achieve the selected size. This sample has a calculated density of 2.73 g/cm^3 , according to the procedures of UNE 80103:2013, here labeled as LFS-F. The particle size distribution and the physical appearance of both as-received LFS samples, obtained with the methodology of UNE-EN 933-1 [60], are shown in Figure 2-1. The chemical composition of the samples was determined by X-ray Fluorescence (XRF) measurements using a Philips spectrometer, model PW2400. XRF results are shown in Table 2-1, which shows that all the materials studied in this work presented similar chemical composition. All samples were rich in Ca and Si and, to a minor extent, in Fe, Al and Mg. Smaller amounts of Mn and S as well as some traces of other elements are also found in the samples. The LFS chemical composition is within the expected ranges for this type of slag according to the literature (see Table 1-1).

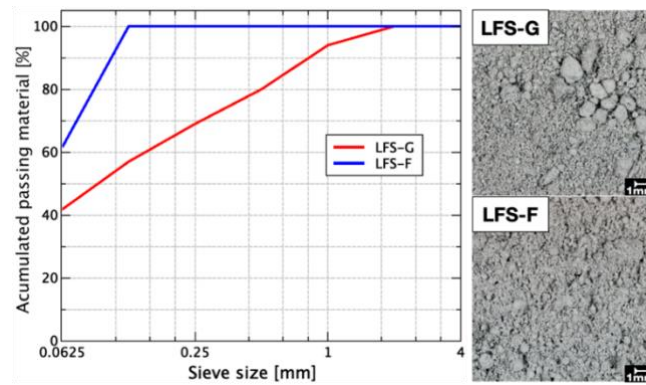


Figure 2-1: LFS particle size distribution.

Both types of LFS exhibit higher total content of Mg and Fe than CEM, which is expected due to the steelmaking process. Furthermore, in the case of Mg content, it is higher in the LFS-F sample than in LFS-G, which can be attributed to the variability of the steelmaking process inside the same plant, as these materials came from different batches. In the case of Fe content, it is higher in the LFS-G sample than in LFS-F. Because, in the material preparation stage the magnetized material was removed with a magnet, in order to reduce the interference of the grounding and sieving process of the LFS to obtain the necessary particle size for microstructural techniques analyses. And therefore, higher amount of material was removed in the LFS-F sample preparation than in LFS-G, so a lower Fe content is expected in the LFS-F samples.

Distilled water was used for the manufacture of the cement paste mixtures. Also, a superplasticizer additive Masterglenium UG 1323 from BASF Construction Chemicals was used to ensure the workability of the cement pastes.

Table 2-1: Chemical composition of raw materials obtained by XRF (in %).

Material	CaO	SiO ₂	Al ₂ O ₃	Fe ₂ O ₃	SO ₃	MgO	MnO	K ₂ O	TiO ₂	Cr ₂ O ₃	BaO	Σ others	LOI
CEM	63.2	18.7	4.0	3.3	2.9	1.4	0.0	0.7	0.2	0.0	-	0.5	5.0
LFS-G	45.6	19.3	6.7	10.8	1.8	5.8	1.7	0.0	0.5	0.8	0.2	0.6	6.2
LFS-F	48.1	20.7	5.6	7.2	1.9	6.6	1.3	0.0	0.4	0.4	0.2	0.5	7.1

2.2 Mix design and sample preparation

To study the effects of LFS as a cement replacement, cementitious pastes were made using 18wt% and 25wt% according to total cementitious material content, for LFS-G and LFS-F respectively. This parameters were selected according to previous studies dealing with LFS cement replacement in concrete mixtures with a fixed 370 kg/m^3 of cementitious material (CM)[61]. For this CM content, a

water to cementitious material ratio (W/CM) of 0.32 was selected, and a final 0.5wt% addition of superplasticizer (related to the CM content) to ensure workability was used to fabricate the cementitious pastes studied. The proposed mixtures for LFS-G and LFS-F cement replacement (here labeled as CPG and CPF respectively) are shown in Table 2-2. Sample CPC corresponds to the control sample using only Portland cement (CEM) without any slag addition.

Table 2-2: Dosage of cementitious pastes (in kg).

MIXTURES	CEM	LFS-F	LFS-G	W
CPC	370	-	-	118
CPG	302	-	161	118
CPF	278	92	-	118

The standardized process described in UNE-EN-196-1 [62] was used to prepare the cement paste batches. After being prepared, the mixtures were poured into $25 \times 25 \times 285 \text{ mm}^3$ prismatic oiled molds. For each batch, three molds were prepared, with each mold containing three prismatic specimens. Three of these were cured in a curing chamber (95% relative humidity and 20°C) for 7, 28, 60 and 315 days. After these periods, the corresponding microstructure characterization and macroscale physical-mechanical properties such as density, absorption and pore volume were determined according to the standard ASTM C642 [63]. While the compressive strength was assessed according to the standard UNE EN 196-1.

The other six prismatic specimens were used to test the macroscale volume instability according to ASTM C1038 [64] and ASTM C490 [65], subjected to 3 types of curing environments: i) curing chamber at 20°C and 95% R.H. (CC); ii) submerged in water inside a sealed container in an oven at 70°C (SW); iii) subjected to 25 autoclave (AC) cycles (one AC cycle corresponds to the sample submitted to 135°C and 2.03 bars of pressure for 5.5 hours, then allowed to cool for 18.5 hours inside the AC to reach ambient temperature). Note that the first 1.5 hours of each cycle is the time needed for the equipment to reach the specified conditions. Finally, after each AC cycle, a length measurement was taken according to ASTM C490.

2.3 Testing procedures

To characterize the as-received raw materials (cement and slags), complementing the chemical data obtained by XRF and to study the evolution of the LFS-cement systems microstructure scanning electronic microscopy with energy dispersive X-rays microscopy microanalysis (SEM/EDX), transmission Fourier transform infrared spectroscopy (FTIR), and powder X-ray Diffraction (XRD) tests were employed. The hydration of the samples was stopped with the solvent exchange method. Then the samples were pulverized to a particle size below 0.063 mm, homogenized and ready to be analyzed with the above-mentioned techniques.

To study the initial hydration reactions of cement pastes with LFS-cement replacement, isothermal conduction and semi-adiabatic calorimetry were conducted. A Calmetrix I-CAL 4000 calorimeter at 20°C. A total of 6 g of binding material with the same proposed dosage as described in section 2.2 were used for isothermal conduction calorimetry. Semi-adiabatic calorimetry experimental setup consists of SQ2020 squirrel datalogger from Grant Instrument and its operating software connected to type K thermocouple. The thermocouple was inserted into the center of the fresh, recently mixed sample poured into a sealed/insulated plastic vessel. The plastic vessel was immediately placed inside an insulated expanded polystyrene container with a capacity of four samples and one control water sample. For both tests, the room temperature was about 20°C, and external hand-mixing for less than two minutes of the paste samples were conducted, helped with a vortex mixer directly in the plastic vials and then loaded into the equipment to measure the heat hydration and the temperature evolution, respectively, for the first 22 hours.

SEM/EDX studies of raw materials and hydrated LFS-cement pastes were realized in a FEI scanning electronic microscopy equipped with energy dispersive X-rays microscopy model ESEM Quanta 200, XTE 325/D8395. SEM/EDX measurements for hydrated LFS-cement pastes were conducted at 60 curing days.

Powder XRD measurements of raw materials and hydrated samples were performed using a Bruker D8-A25 Diffractometer equipped with a Cu X-ray source (CuK α radiation, 40 kV and 40 mA working conditions) and a LynxEye position sensitive detector. A thin Ni foil was used to filter out the CuK β radiation. All scans were acquired between 4° and 80° in 2 θ with a 0.019° step size, and a counting time of 0.8 s per step. Phase identification was carried out by using the DIFFRAC EVA software together with the ICDD PDF-2 database and the Crystallography Open Database (COD). Quantitative phase analysis of the XRD scans (QXRD) was performed with the Rietveld refinement method after spiking the samples with 10wt% of zincite, which acts as an internal standard. The Rietveld analyses were performed with the TOPAS v4.2 software from Bruker. Structural information (unit cell, atomic positions) for the different mineral phases was taken from Ref. [66] and, in some cases, from the COD database or the American Mineralogist Crystal Structure Database (AMCSD) [67]. Powder XRD measurements for hydrated LFS-cement paste were conducted at 7, 28, 60, and 315 curing days.

Room-temperature FTIR transmission scans for all the samples studied in this work (raw materials and hydrated LFS-cement pastes) were acquired using a Bruker Vertex 80v spectrometer, using OPUS v5.5 spectroscopic software to analyze the results. Each FTIR spectra were acquired with 32 scans, with a spectral resolution of 2 cm⁻¹ over a range of 4000-380 cm⁻¹. The KBr pellet technique was used for the FTIR test, with KBr pellets containing 1wt% of the sample. FTIR transmission measurements for hydrated LFS-cement paste were conducted at 7, 28, and 60 curing days.

To study the effect of LFS as a cement replacement at the macroscopic level, density and porosity were determined according to ASTM C642. Compressive strength tests were conducted according to UNE EN 196-1 at 7, 28, 60, and 315 curing days. Volume instability was measured according to ASTM C490-04 and ASTM C1038 until 315 curing days for the samples exposed to CC and SW curing environment, or after each of the 25 autoclave cycles.

3 Results and discussion

3.1 Raw materials characterization

3.1.1 SEM

The SEM/EDX characterization of the CEM sample shows typical anhydrous cement phases such as C₃S / C₂S, C₄AF, calcite, and gypsum. Figure 3-1 shows SEM images of typical phases observed in LFS samples, such as (a) a calcium silicate phase, probably C₂S polymorph, due to its rounded shape, high content of Ca and Si, and some trace elements or impurities like Fe, Mg, Al, or S, which are commonly found in slags; (b) a phase with high content of Ca and O and traces of Si and Mg, but without any characteristic shape; it could correspond to calcite or portlandite, since both phases have been identified by FTIR and XRD in LFS samples; (c) periclase, due to the high content of Mg and O; (d) wüstite grains, with a high content of Fe, O and small amounts of Ca, Mn as well as some traces of other elements (Al, Si, Mg and Cr); (e) gehlenite irregular grains, with high content of Ca, Si, Al, and traces of Mg, S, and Fe; (f) euhedral merwinite microcrystals, with a regular shape and high content of Mg, Ca and O, small amounts of Si and traces of Al and Mo.

3.1.2 XRD

Selected XRD scans of as-received cement and slags samples, between 5° and 65° in 2 θ , are shown in Figure 3-2. The CEM sample exhibits typically crystalline phases found in this type of anhydrous cement including C₃S, β -C₂S, C₄AF, C₃A, gypsum, and calcite. Both slags presented a similar qualitative mineralogical composition, as expected (same plant, different batch). These results are in agreement with the literature [21,23,54] and confirm the SEM/EDX results. It is observed the

presence of reactive phases such as β -C₂S, periclase and mayenite. Also, it is crucial to notice the absence of free CaO, indicated with dotted black lines in Figure 3-2, and the presence of hydration and carbonation products like portlandite and calcite due to the rapid consumption of free CaO in the weathering/maturity process. Furthermore, the presence of brucite is detected, which can probably be attributed to a slower kinetics reaction of free MgO in the weathering/maturity process. Finally, low/non-reactive compounds such as γ -C₂S, gehlenite, merwinite, and wüstite are found. It is important to highlight the absence of free CaO and the remaining presence of free MgO, as these two phases are the main products to cause volumetric instability problems in LFS-cement systems.

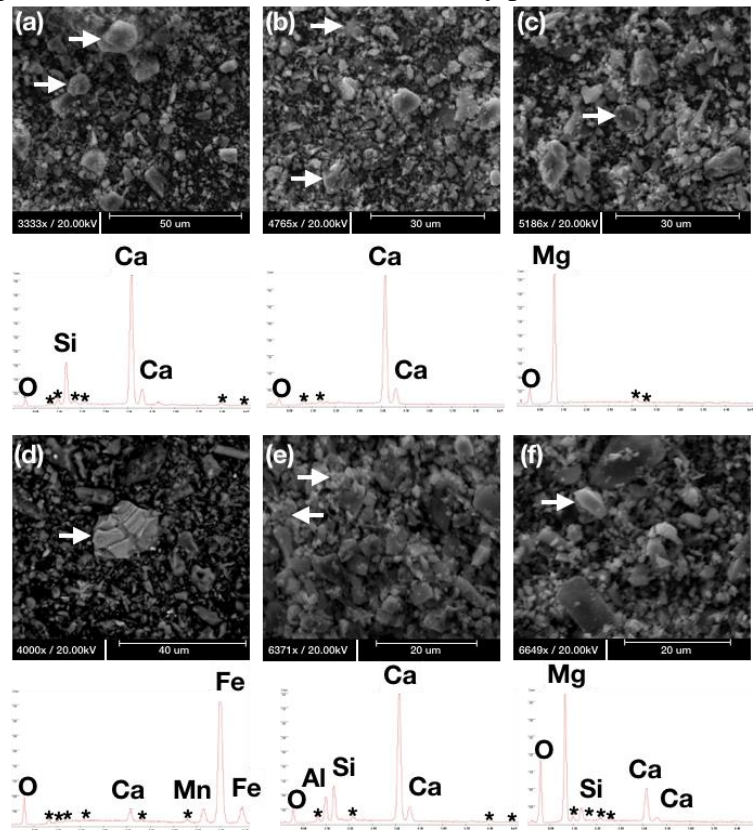


Figure 3-1: SEM micrographs and EDX microanalysis of as receive LFS samples LFS-G and LFS-F (a) C₂S, (b) portlandite/calcite (c) periclase, (d) wüstite, (e) gehlenite, (f) merwinite.

3.1.3 Rietveld refinement

The quantitative mineralogical compositions of the as-received samples identified by Rietveld refinement are shown in Table 3-1. The silicate and aluminate phases identified in the CEM sample are found within the expected ranges: C₃S (56.2%), β -C₂S (14.5%), C₄AF (11.0%), and C₃A (4.0%). The total weight content of phases like gypsum and calcite are 4.8% and 9.2%, respectively. Both LFS samples (LFS-G and LFS-F) exhibit a similar, although not identical, quantitative mineralogical composition. The majority phases correspond to C₂S polymorphs (γ -C₂S and β -C₂S) with more than 30%, followed by merwinite, gehlenite, and periclase between 5% - 10%, then calcite around 4% and finally wüstite, portlandite, and mayenite with approximately 1% - 3%. Minor/traces phases with less than 1% are also detected (quartz and brucite). Finally, the total content of amorphous phases inferred in both LFS samples is around 40%.

It is essential to notice that no free CaO is detected in both LFS samples, where a very low content of portlandite and a higher amount of calcite is found. Since LFS is exposed to a weathering/maturity process, problematic phases like CaO were probably converted through hydration/carbonation into portlandite and calcite. Nevertheless, free MgO is still present in these samples due to slower hydration and carbonation kinetics. Therefore, this phase is a key factor that needs to be controlled

for the use of LFS as cement replacement, because it is one of the critical phases that could show expansion problems when hydrated. Some important differences between LFS mineralogical composition samples are the reactive phases β -C₂S and periclase. The content of these two phases is higher in LFS-G, while their corresponding hydration/carbonation products (portlandite, amorphous phase, and brucite) are higher in LFS-F. In both cases the differences could be related to the variability of the steelmaking process within the same plant among different batches, but also due to a higher reactivity of LFS-F owing to its smaller particle size distribution.

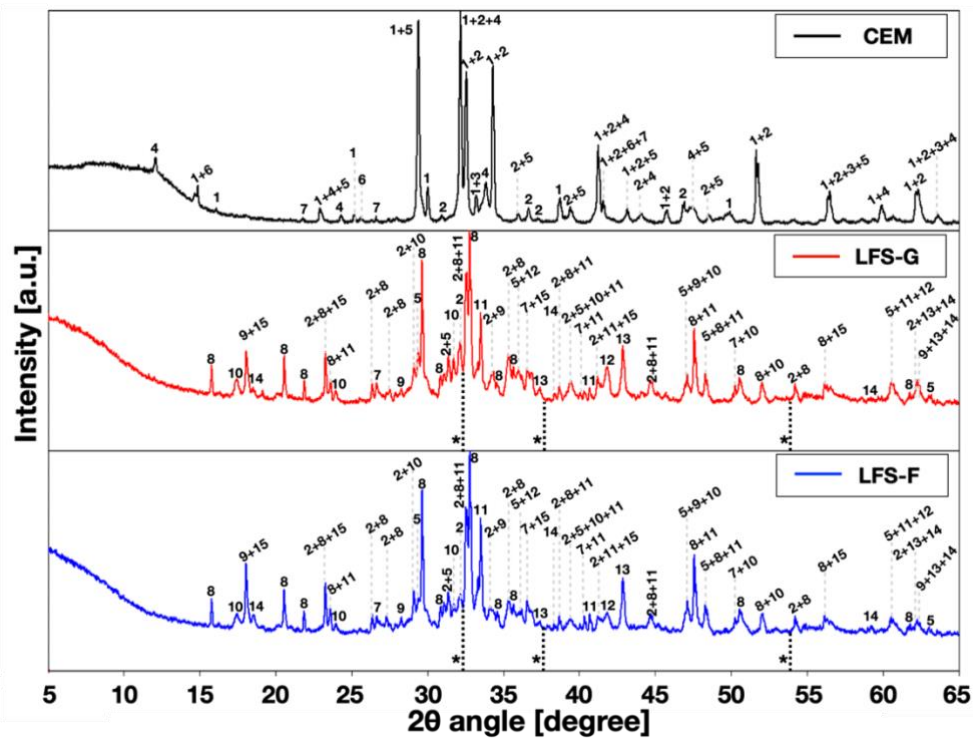


Figure 3-2: XRD diffractograms of cement, LFS-G and LFS-F raw materials, with the characteristic CaO peaks in dotted black line, where: (1) C₃S; (2) β -C₂S; (3) C₃A; (4) C₄AF; (5) calcite; (6) gypsum; (7) quartz; (8) γ -C₂S; (9) portlandite; (10) gehlenite; (11) merwinite; (12) wüstite; (13) periclase; (14) brucite; (15) mayenite; (*) lime.

Table 3-1: Mineralogical composition of raw materials

Mineralogical Phase	ID	Mineralogical composition [%]		
		CEM	LFS-G	LFS-F
C ₃ S	1	56.2	-	-
β -C ₂ S	2	14.5	12.1	9.1
C ₃ A	3	4.0	-	-
C ₄ AF	4	11.0	-	-
Gypsum	6	4.8	-	-
Calcite	5	9.2	4.2	3.7
Quartz	7	-	0.7	0.5
γ -C ₂ S	8	-	19.8	22.4
Gehlenite	10	-	7.3	4.9
Merwinite	11	-	7.3	9.8
Mayenite	15	-	1.4	1.6
Periclase	13	-	5.7	4.4
Portlandite	9	-	1.5	2.2
Wüstite	12	-	2.6	1.6
Brucite	14	-	0.2	0.2

3.1.4 FTIR

The FTIR characterization of CEM sample (described in Appendix A) shows the presence of typical anhydrous cement phases such as C_3S , C_2S , C_3A , C_4AF , calcite, and gypsum confirming SEM/EDX and XRD results. FTIR spectra of raw LFS samples, LFS-G and LFS-F, are shown in Figure 3-3(a-b), respectively. Both slags are very similar, and exhibit typical LFS phases, only with minor differences in the intensities of some peaks, as expected due to their common origin and similar mineralogical composition.

These spectra are dominated by a characteristic wide band between 800 and 1100 cm^{-1} due to the vibrations of the Si-O and Al-O bonds. These bands are formed by the overlapping of FTIR signals from different C_2S polymorphs [68,69] and also from merwinite/gehlenite/mayenite. Similarly, to the CEM sample, the band over 500 cm^{-1} is also visible, with a central peak attributed to the vibrations of Si-O and Al-O bonds. However, this band exhibits a shoulder to higher and lower wavenumbers, which could be related to the presence of merwinite in the LFS addition [70]. In turn, calcite can be identified through its characteristic peaks at 700 and 1800 cm^{-1} , and the band above 1500 cm^{-1} [68,71]. This band reveals a minor peak displacement and broadening to higher wavenumbers that could be related to the vibration of the Mg-O bonds in periclase/brucite [17,21]. The broadening of the band over 500 cm^{-1} could be related to the vibration of the Fe-O bonds of wüstite [72]. Two additional peaks are visible in these spectra: first, a well-defined feature at 1630 cm^{-1} and, second, a wider/broader peak that appears as a hump in the baseline around 3500 cm^{-1} . These two features are characteristic of the OH group in water arising from the hydrated components of LFS [17,68,69]. Finally, it is worth noticing the two additional peaks located at around 3640 and 3700 cm^{-1} , which correspond to the vibration of the OH group in portlandite [17,68,69] and brucite [2,68,73], respectively. These results are particularly interesting because they confirm the absence of free CaO and the presence of brucite, therefore demonstrating that the LFS is in a higher state of maturity due to weathering, with a portion of the dangerous expansive phases CaO and periclase already consumed.

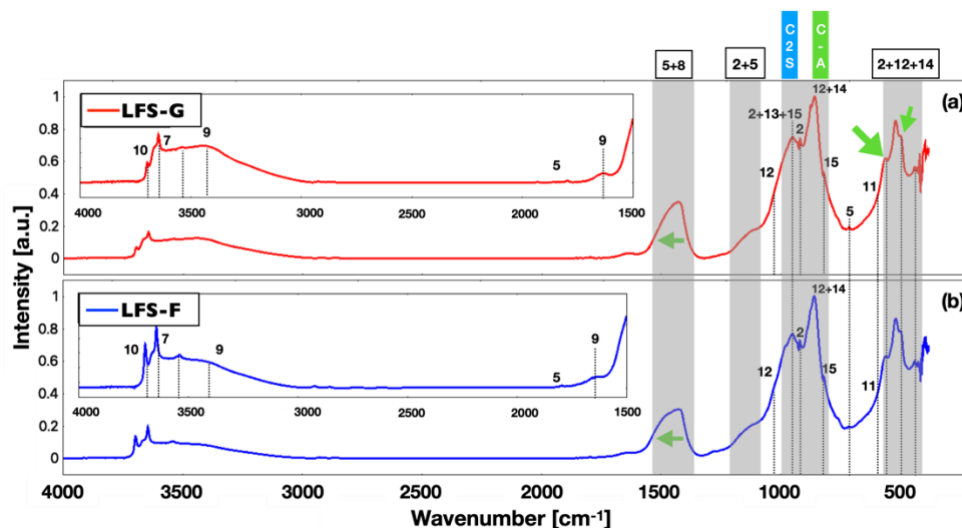


Figure 3-3: FTIR spectra of LFS-G and LFS-F raw materials where: (2) β - C_2S ; (5) calcite; (7) portlandite; (8) periclase; (9) C-S-H gel; (10) brucite; (11) wüstite; (12) merwinite; (13) gehlenite; (14) mayenite; (15) γ - C_2S .

3.2 Early hydration reactions

3.2.1 Isothermal and semi-adiabatic calorimetry

Figure 3-4(a,b) shows the results of hydration kinetics with isothermal conduction calorimetry and Figure 3-4(c) with semi-adiabatic calorimetry for all the cement pastes studied in this work.

In Figure 3-4(a), the initial hydration period (0–1 h) appears as a narrow peak associated with the dissolution and induction period (stage I and II) [74]. The hydration heat evolution rate at this stage in CPG sample increased over CPC and CPF samples, due to the fact that the low reactivity of LFS-G and the extra material added (58% > 0.063 mm) leads to higher effective water to cement ratio and promotes the dissolution and hydration of cement particles. The CPF sample shows the lowest heat evolution rate of all samples, because of the low reactivity of the LFS-F compared to cement but with a higher SSA than LFS-G. Thus, there is a higher demand of water in this case, resulting in lower effective water to cement ratio. As the hydration went on as shown in Figure 3-4(b,c), it continued with the dormant period (stage II) reaching the lower values of heat flow and temperature. The dormant period appears to be prolonged with both LFS-F and LFS-G replacement, thus delaying the start of stage III. This latter stage corresponds to the accelerating period, which is characterized by a clear change of slope and a rapid increase of heat flow and temperature, associated to the initial set of setting time. Also, the LFS replacement produced a decrease and delay of C₃S hydration peak, presented as the highest point of the heat flow and temperature curves. This effect is associated to the dilution effect of cement with the LFS replacement, decreasing the total amount of C₃S. The CPF sample also presented an increase of C₃A hydration peak, even higher than the C₃S. Seen as an increased peak after the C₃S peak around 10 hours, associated with the hydration of the extra aluminates, such as mayenite, added with the LFS-F replacement. This effect is not so clear in the CPG sample related to the lower SSA and lesser reactivity of LFS-G.

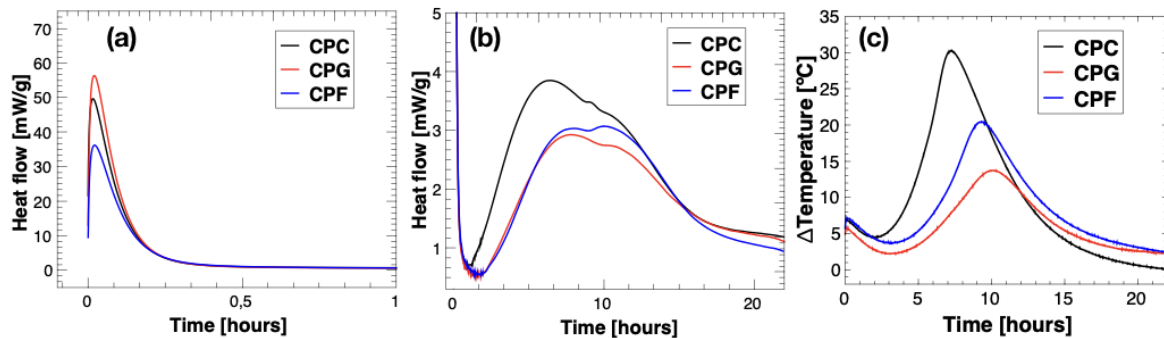


Figure 3-4: Isothermal and semi-adiabatic calorimetry test for all the cement samples.

3.3 Microstructural characterization of LFS-cement hydrated systems

3.3.1 SEM

Figure 3-5 and Figure 3-6 show SEM/EDX micrographs together with chemical microanalysis of cement pastes samples CPG, and CPF at 60 curing days, respectively. Both figures show some of the expected CEM-LFS systems phases, similar to what occurs in CPC sample (described in Appendix B).

Figure 3-5(a) and Figure 3-6(a), shows a semi-hydrated cement grain with an irregular shape, high content of Ca, Si, in CPG and high content of Ca, Al and Fe in CPF samples. A lighter grayscale tone at the center related to anhydrous cement phases surrounded by a darker grayscale tone halo corresponding to the recently formed amorphous hydrated phases C-S-H gel. Furthermore, it could be observed some of the non-reactive phases of LFS such as wüstite with a high Fe, O content and irregular shape (see Figure 3-5(b)); a calcium silicate rich phase, probably γ -C₂S with a regular shape and high content of Ca and Si similar to semi-hydrated cement grains but in this case, with the absence of the darker halo of hydrated phases around it (see Figure 3-5(c)); a gehlenite phase with a high content of Ca, Al and Si, and as well as γ -C₂S the lack of hydration products around it, because it does not present hydraulic activity (see Figure 3-6(b)). Also, it could be observed the presence of some hydrated products like calcite surrounded by the amorphous phase (see Figure 3-6(c)).

Figure 3-5(d) and Figure 3-6(d) show a macropore for CPG and CPF samples, respectively, but with a less clear image of the different phases, like portlandite and calcite, that are observed on the macropores surface in the CPC sample (see appendix B). This difference marked by a diffuse amorphous matrix that covers the entire surface of the pore. Not allowing to identify other hydrated products, even more diffuse in the case of the CPF sample. Could be explained by the sum of the LFS filler effect that acts as a nucleation site in the hydration reactions, and the increased shearing condition by the solid non-reactive particles of LFS in the mixing that favors the formation of C-S-H gel in the space between particles rather than over cement particles [74].

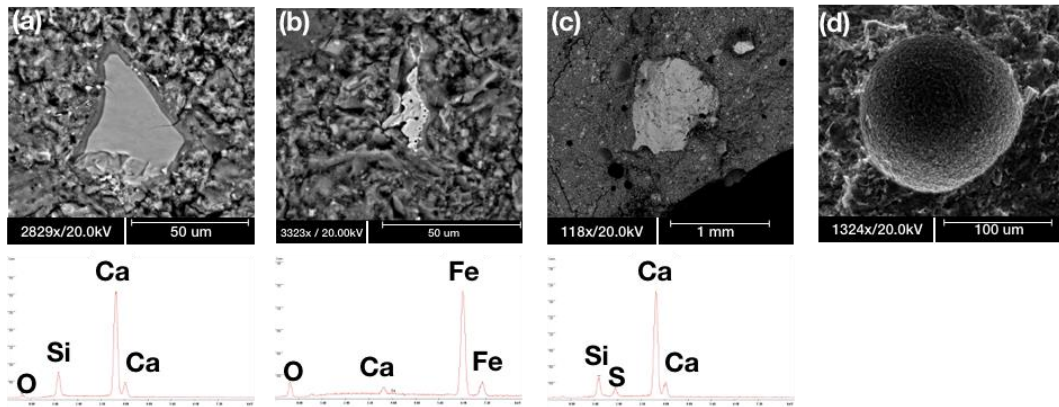


Figure 3-5: SEM micrographs and EDX microanalysis of CPG sample at 60 curing days (a) semi hydrated cement grain, (b) wüstite, (c) γ -C₂S, (d) CPG macropore.

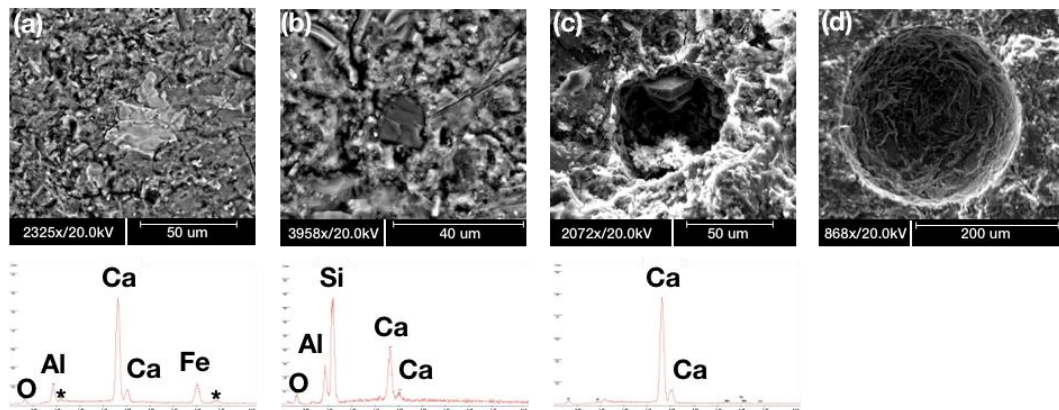


Figure 3-6: SEM micrographs and EDX microanalysis of CPF sample at 60 curing days (a) semi hydrated cement grain, (b) gehlenite, (c) calcite formation, (d) CPF macropore.

3.3.2 XRD

The mineralogical composition of the hydrated LFS-cement system samples at 7, 28, 60, and 315 days are shown in Figure 3-7 and Figure 3-8, for CPG and CPF respectively.

Both samples exhibit a similar behavior than the CPC sample (described in appendix B) after 7, 28, 60, and 315 days. Mostly a combination of anhydrous CEM and LFS phases and the typical evolution of hydration products in cement pastes with an initial formation of AFt, calcite, portlandite and, at later ages, the formation of carboaluminate in combination with the consumption of C₃S, β -C₂S, C₃A and gypsum. Therefore, indicate that the hydration reactions of Portland cement are those that control the hydration reactions and development of new phases in this cementitious matrix (LFS-CEM systems).

There is however an evident dilution effect of minor phases in LFS observed as a weakening/disappearing of some reflections. Also, phases from the anhydrous CEM sample, like C₃S, C₂S and C₄AF, the non-reactive phases in LFS such as γ -C₂S, gehlenite, or merwinite, are still visible after

315 days (see Figure 3-7 and Figure 3-8). It should be stressed that in all the diffractograms (CPG and CPF), a sort of displacement of the baseline in the form of a curvature or hump is visible between 25° to 40° in 2θ. It is well known that this XRD signal is characteristic of the amorphous phase "C-S-H gel" that is formed during the hydration reactions of these LFS-CEM systems.

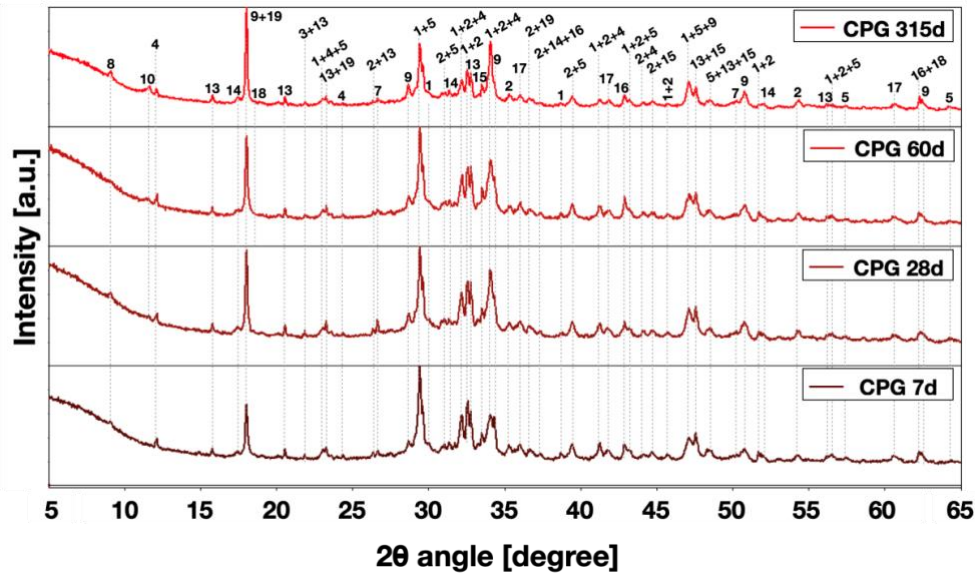


Figure 3-7: CPG diffractograms at 7, 28, 60 and 315 curing days where (1) C3S; (2) β-C2S; (4) C4AF; (5) calcite; (7) quartz; (8) AFt; (9) portlandite; (10) carboaluminate; (13) γ-C2S; (14) gehlenite; (15) merwinite; (16) periclase; (17) wüstite; (18) brucite; (19) mayenite.

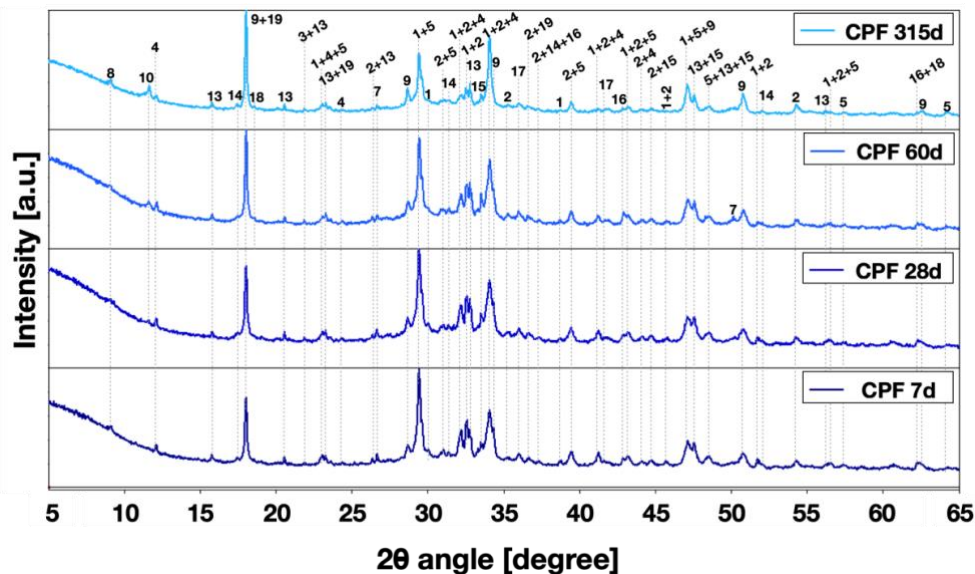


Figure 3-8: CPF diffractograms at 7, 28, 60 and 315 curing days where (1) C3S; (2) β-C2S; (4) C4AF; (5) calcite; (7) quartz; (8) AFt; (9) portlandite; (10) carboaluminate; (13) γ-C2S; (14) gehlenite; (15) merwinite; (16) periclase; (17) wüstite; (18) brucite; (19) mayenite.

3.3.3 Rietveld refinement

The quantitative mineralogical composition evolution of CPC, CPG, and CPF samples is shown in Table 3-2 to Table 3-4, respectively. The column for 0 curing days for CPC sample corresponds to the anhydrous CEM sample, whereas for the CPG and CPF samples this column corresponds to the mass weighted sum of its anhydrous components. These values provide us with a starting-point compositional values for monitoring the hydration reactions of the different mixtures. For the CPC sample, a rapid initial consumption of the cement components C₃S (56wt% to 8wt%), C₃A (4wt% to

1wt%) and gypsum (5wt% to 0wt%) is observed, together with the appearance of the hydration products AFt (2wt%), portlandite (7wt%) and an amorphous phase “C-S-H gel” (56wt%). Also, a lower consumption rate of β -C₂S and C₄AF phases is observed relative to C₃S. At later ages, the formation rate of the amorphous phase changes and becomes slower due to the lower reactivity of β -C₂S and the consumption of the accessible components. Finally, these data provide an estimation of the fraction of anhydrous CEM phases that still remain after 315 curing days. At the (theoretical) 0-day starting point for CPG and CPF samples, it could be observed a dilution effect of the main components in Portland cement and LFS with the cement replacement. In the cement-slag mixture, C₃S and β -C₂S contents are lower than the control sample. As hydration occurs the behavior of CPG and CPF samples is similar to CPC sample, with a fast consumption of the reactive components contributed by both Portland cement and LFS (C₃S, β -C₂S, C₃A, C₄AF, and gypsum). While the typical hydration products are formed (portlandite, AFt, carboaluminate, and amorphous phase “C-S-H gel”), limited participation of the slow reactive LFS phase periclase, with very low brucite formation (less than 1% in both samples), is observed, which is probably due to the slower hydration kinetics of this phase. As expected, the non-reactive phases γ -C₂S, merwinite, gehlenite, and wüstite have a very low variation in all the ages analyzed, so they would not contribute to the formation of new products in the hydration process and would only participate as a filler. The amount of hydration products is lower in LFS-cement samples compared to CPC, reflecting the dilution effect of cement. Specially, if the initial amorphous phase contribution by LFS is discounted, and not overestimated the principal strength gain component formed in the hydration reactions (C-S-H gel from LFS-cement systems) due to the initial input of amorphous phase identified in the QXRD (see Table 3-3 and Table 3-4), so at least 10% of the amorphous phase is non-reactive and probably acting only as a filler.

Table 3-2: CPC QXRD

MINERALOGICAL PHASE	ID	CURING DAYS				
		0	7	28	60	315
C ₃ S	1	56.2	7.7	6.5	5.4	4.2
C ₄ AF	4	11.0	4.1	4.5	4.6	4.7
β -C ₂ S	2	14.5	7.8	8.0	7.4	6.6
C ₃ A	3	4.0	0.8	0.3	0.2	0.1
Calcite	5	9.2	15.5	16.1	15.1	11.4
Gypsum	6	4.8	0.0	0.0	0.0	0.0
Portlandite	9	-	6.5	8.3	8.6	11.0
Ettringite	8	-	1.6	1.5	2.3	1.5
Carboaluminate	10	-	-	-	0.2	0.5
Amorphous phase	-	-	56.0	54.9	56.0	60.0

Table 3-3: CPG QXRD

MINERALOGICAL PHASE	ID	CURING DAYS				
		0	7	28	60	315
C ₃ S	1	36.5	7.7	6.0	5.5	4.7
β -C ₂ S	2	13.6	7.6	7.4	6.3	3.1
C ₃ A	3	2.6	0.0	0.0	0.0	0.0
C ₄ AF	4	7.1	3.9	3.9	3.7	3.7
Gypsum	6	3.1	0.0	0.0	0.0	0.0
Calcite	5	7.5	14.7	12.3	11.3	9.7
Quartz	7	0.2	0.3	0.3	0.1	0.1
γ -C ₂ S	13	6.9	8.6	8.0	7.4	7.5

Gehlenite	14	1.8	2.7	2.7	2.7	2.5
Merwinite	15	2.6	2.5	1.6	1.6	1.4
Mayenite	19	0.5	0.5	0.4	0.2	0.1
Wüstite	17	0.9	<DL	<DL	<DL	<DL
Periclase	16	2.0	2.5	2.3	2.2	1.8
Brucite	18	0.1	<DL	<DL	<DL	<DL
Portlandite	9	0.6	4.2	5.2	6.0	7.5
Ettringite	8	-	1.3	1.5	1.2	1.3
Carboaluminate	10	-	-	-	0.7	2.9
Amorphous phase	-	13.9	43.5	48.4	51.1	53.7

*<DL correspond to below detection limit

Table 3-4: CPF QXRD

MINERALOGICAL PHASE	Code	CURING DAYS				
		0	7	28	60	315
C ₃ S	1	42.1	7.2	5.5	4.3	3.7
β-C ₂ S	2	13.2	5.5	5.2	4.1	1.9
C ₃ A	3	3.0	0.0	0.0	0.0	0.0
C ₄ AF	4	8.2	3.5	3.7	3.6	3.3
Gypsum	6	3.6	0.0	0.0	0.0	0.0
Calcite	5	7.9	15.5	13.1	13.2	9.5
Quartz	7	0.1	0.1	0.2	0.1	0.1
γ-C ₂ S	13	5.6	6.7	7.0	7.5	6.6
Gehlenite	14	1.2	1.9	2.3	1.8	1.6
Merwinite	15	2.5	1.3	1.7	1.5	1.4
Mayenite	19	0.4	0.1	0.2	<DL	<DL
Wüstite	17	0.4	<DL	<DL	<DL	<DL
Periclase	16	1.1	1.0	1.1	1.0	0.8
Brucite	18	0.0	<DL	<DL	<DL	<DL
Portlandite	9	0.6	5.8	5.6	7.0	9.5
Ettringite	8	-	1.6	1.2	0.9	1.3
Carboaluminate	10	-	-	-	0.6	4.2
Amorphous phase	-	9.9	49.8	53.2	54.4	56.1

*<DL correspond to below detection limit

3.3.4 FTIR

FTIR transmission spectra of slag-cement pastes CPG and CPF at 7, 28, and 60 curing days are shown in Figure 3-9 and Figure 3-10, respectively. Both samples do not show sizable differences relative to the evolution of CPC sample (described in appendix B).

In these samples the FTIR spectra confirm that the hydration processes of Portland cement govern the LFS-cement system reactions. The characteristic peaks due to the formation of hydrated amorphous phase C-S-H gel (OH peaks at 3500 and 1630 cm⁻¹), the increase of portlandite (see Figure 3-9(a) and Figure 3-10(a)) and calcite phases, and the transient appearance of AFt and AFm phases (see Figure 3-9(b-c) and Figure 3-10(b-c)). The formation of other new phases is not evident in these FTIR spectra. Also, show some differences related to the intensities and evolution of the peaks associated with the hydrated phases. The amorphous phase evolution in CPG sample presented an age dependence, as observed in CPG 7d spectrum. The sample shows a lower overall intensity, related to a less reactive LFS and the overall reduction of C₃S content due to the dilution cement effect, that decreases the early age formation of C-S-H gel and portlandite. However, at latter ages β-C₂S from cement and LFS-G could hydrate and contribute to the formation of hydrated phases as

presented for CPG 28d and 60d spectra. In contrast, the CPF sample seems to exhibit a rapid increase, but without any age dependence. This could be associated with the initial contribution of amorphous hydrated phases from LFS-F to the mixture, a lesser dilution effect of cement than LFS-G, and a higher filler effect due to its smaller particle size. At later ages, there seems to be a minor stall/decrease in the formation of hydrated phases associated with the rapid consumption of the available reactive phases and the dilution effect of cement.

Another important difference observed in these two samples is the presence of brucite and its evolution with respect to curing time. Brucite is detected with a characteristic peak around 3700 cm^{-1} [73], located at higher wavenumbers than the characteristic peak of portlandite, as presented in Figure 3-9(a) and Figure 3-10(a). This feature is more intense in the CPF than in the CPG sample, and maintains a dependence over time, with a slight increase in intensity as curing time pass.

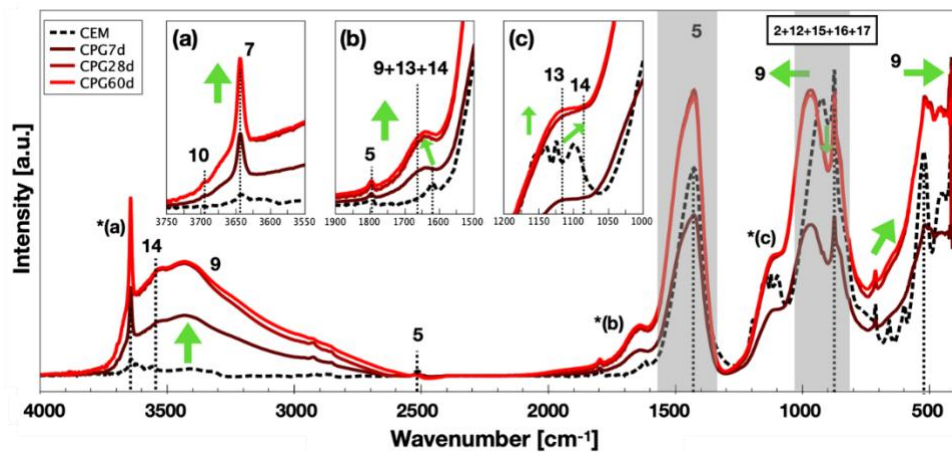


Figure 3-9: CPG FTIR spectra at 7, 28 and 60 curing days where: (2) β - C_2S ; (5) calcite; (7) portlandite; (9) C-S-H gel; (10) brucite; (12) merwinite; (13) AFt; (14) AFm; (15) γ - C_2S ; (16) gehlenite; (17) mayenite.

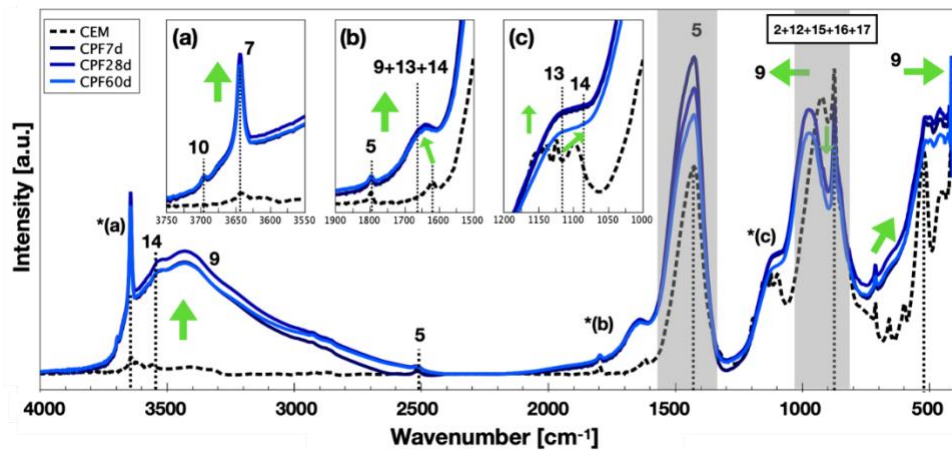


Figure 3-10: CPF FTIR spectra at 7, 28 and 60 curing days where: (2) β - C_2S ; (5) calcite; (7) portlandite; (9) C-S-H gel; (10) brucite; (12) merwinite; (13) AFt; (14) AFm; (15) γ - C_2S ; (16) gehlenite; (17) mayenite.

3.4 Evolution of physical-mechanical properties

The evolution of physical-mechanical properties for all the hydrated pastes studied in this work (CPC, CPG and CPF) can be seen in Figure 3-11. Figure 3-11(a) shows the measured densities as a function of age, all samples displayed values in the expected range (1.7 to 1.9 g/cm^3). CPG has the highest density, and CPF has the lowest density of all samples analyzed. This is contrasted in Figure 3-11(b) with the porosity results, which show that CPG has the lowest pore volume, while CPF has the highest pore volume of all studied samples, with values in the range of 27% to 35%. For CPG, this is due to the evolution of hydration reactions, the recently formed phases have larger volume

than the anhydrous phases, occupying the free space available. Also, to the extra 58% of LFS-G material that was added to the mix with sizes between the fractions of 0.063 and 2 mm. This material corresponds to the coarse particles of LFS-G, with no cementing activity, and may be playing an important role as a filler in the slag-cementitious matrix, generating densification of the system. In the case of the CPF sample, LFS-F also has a lower density than CEM, but with no extra material added because it is assumed that all the material had cementing activity. Figure 3-11(c) shows the compressive strength results for all the samples at 7, 28, 60, and 315 curing days. CPC sample obtained the best performance with a compressive strength of 66.5 MPa, 82.8 MPa, 90.1 MPa, and 113.3 MPa, respectively. LFS replacements show a decrease in the mechanical performance compared to the control sample summarized in Table 3-5 due to the dilution cement effect that is caused by decreasing the cement content in the pastes with the LFS replacement, as observed in QXRD results. CPF presents a better performance than the CPG sample, because LFS-F has a smaller particle size and higher SSA than the LFS-G, i.e., a greater reactivity improving the hydration process, acting as a nucleation site and densifying the material. In the case of the CPG sample, this phenomenon can also occur, but to a lesser extent, given the larger particle size and smaller SSA of LSF-G. These characteristics could be related to the lower amorphous phase and portlandite formation for LFS replacement samples observed in the QXRD results. As indicated in ASTM C618 [75] and EN:450-01 [76], the activity index for 28 days must be at least 75% of the compressive strength, so in this case, only CPF approved this limit. However, for older ages, EN:450-01 indicates that for 90 days, this index must be at least 85%. Since it was not controlled in the present work, and at 315 curing days, the CPF sample presented an activity index of 84%. It could be inferred that the CPF sample also achieves this limit, but for the CPG sample this index continued below the limit.

Table 3-5: Compressive strength performance compared to CPC sample

Curing days	CPC [MPa]	Std. Deviation [MPa]	CPG [%]	CPF [%]
7	66.5	9.2	84	97
28	82.8	4.6	67	90
60	90.1	7.4	80	88
315	113.3	7.1	75	84

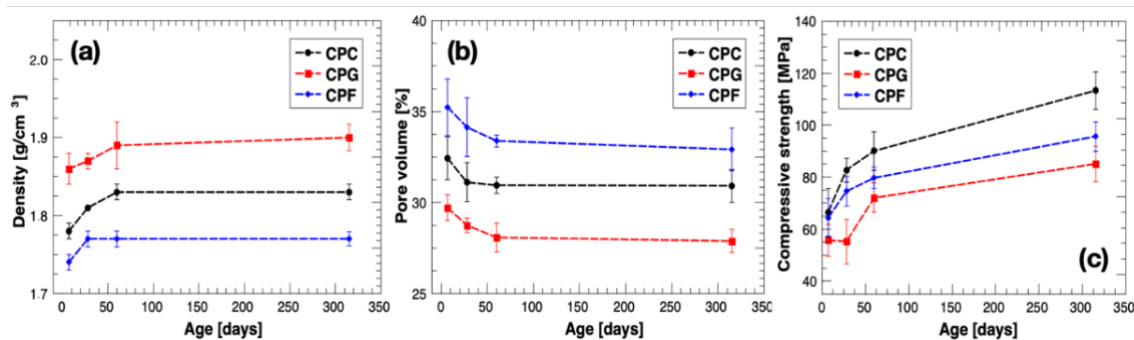


Figure 3-11: Physical-mechanical evolution properties of the cement paste samples at 7, 28, 60 and 315 days (a) density; (b) porosity; (c) compressive strength.

Considering the evolution of the compressive strength of CPC, a rapid increase in strength at an early age (7 and 28 days) is observed, with a rate reduction at older ages (60 and 315 days). This corroborates the results obtained in the microstructural characterization with XRD, QXRD, and FTIR. These techniques showed a rapid initial formation of the amorphous phase and consumption of C_3S , C_3A , and gypsum. Then, at 28 days, this formation and consumption of phases decrease. The CPF sample shows a similar behavior as curing time passes, an increase in strength occurs more

pronounced at an early age (7 to 28 days) then, although this increase in strength is maintained, it occurs at a lower rate (change of slope in the graph). Similar to the CPC sample, due to hydration of anhydrous cement phases (C_3S) and the contribution of the LFS-F that would act as a filler, improving the hydration process. Then at older ages, the β - C_2S phase present in both cement and LFS-F begins to hydrate and contributes to strength gaining. This again corroborates the results obtained with the microstructural characterization by FTIR, XRD, and QXRD, which showed sizable increases in the amorphous phase and consumption of the cement and slag components. Also, the phases that are not reactive are found to remain almost constant. With the CPG sample, the dilution effect of cement content is higher, and the filler effect is lower, producing a lower contribution to strength gain at an early age. Therefore, it does not show a considerable increase from 7 to 28 days. As time passes, the β - C_2S phase present in LFS-G and cement begins to react, producing a contribution in strength gain, which is observed as an increase in strength from 28 curing days to 60 and 315 curing days. These results are corroborated by observing the amorphous phase content at an early age, being the smallest of the three samples in both QXRD and FTIR. Then, the amorphous phase increases to 28, 60 and 315 curing days to achieve greater strength.

3.5 Volumetric instability

The volumetric instability behavior was measured as the linear expansion over time in three types of curing environments CC (inside curing chamber), SW (submerged in water at 70°C) and AC (autoclave) up to the age of 315 curing days for CC and SW, and 25 autoclave cycles for AC samples. In the present work, an arbitrary tolerance limit of 1.0 mm/m has been established for the measured volumetric instabilities, as this value is considered as an acceptable limit for the expansion of structural mortars [35].

Figure 3-12 shows the behavior for the different types of cement pastes at the CC curing environment (CPC, CPG, and CPF), where all samples show an expansion tendency during the controlled time. CPC and CPG samples have very similar expansion behavior, reaching maximum values of approximately 0.6 mm/m at 112 days and 0.8 mm/m at 315 days. The CPF sample, on the other hand, had a maximum expansion of 1.0 mm/m and 1.1 mm/m at 112 days and 315 days, respectively. This expansion tendency could be associated to 2 different effects: first, it must be considered that all samples in CC environment with >95% R.H. are subject to limited evaporation and moisture loss, so drying shrinkage is avoided. Instead, with these optimum conditions for hydration there will be a moisture gain, all pores get saturated, and the hydration reactions continue resulting in an increase in volume or swelling. The second effect for this expansion tendency in cement-slag systems is related to changes in LFS mineralogical composition. As observed with the remaining presence of free MgO in the as-received LFS samples, and the formation of brucite over time due to the hydration of this phase, this last being more pronounced in the CPF sample than in the CPG (see Figure 3-10(a)). These changes produce an increase in volume that may be responsible for part of the linear expansion observed in this type of curing environment for the CPF sample. For CPG sample, in contrast, this expansive behavior did not occur. Because the LFS-G had a bigger particle size than LFS-F, therefore, more difficult to penetrate by water in the hydration process and a smaller SSA which makes it less reactive. Also, there is not enough time to manifest the expansive process due to the lower hydration kinetics of free MgO, expressed in a less pronounced appearance of brucite peaks in the FTIR spectra of CPG (see Figure 3-9(a)).

Figure 3-13 shows the behavior for the different types of cement pastes at the SW curing environment (CPC, CPG, and CPF), where it is observed that all samples show an expansion tendency during the controlled time. The CPC sample has the lowest linear expansion values reaching 0.19 mm/m at 112 days and 0.21 mm/m at 315 days, then CPG sample with a linear expansion close to 0.6 mm/m at 112 days and 0.8 mm/m at 315 days, and finally CPF sample with a maximum of 1.0 mm/m linear expansion at 112 days and 1.2 mm/m at 315 days. After 40 days, CPC sample exhibits some shrinkage/retraction. This could be associated to a lixiviation process due to

597 the fact that the sample was submerged in water, reaching a balance approximately after 100 days,
 598 when the shrinkage/retraction stops and resumes the expansion trend.

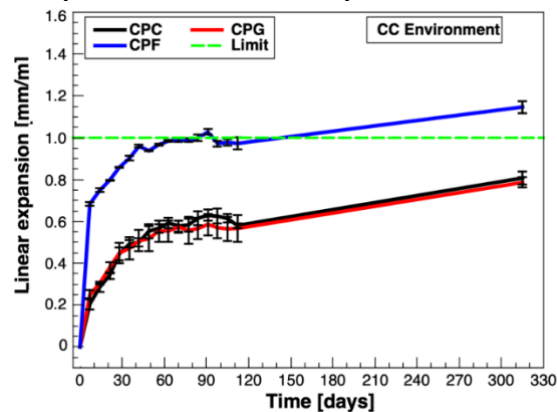


Figure 3-12: Volumetric instability of samples cured in CC environment.

601 CPG and CPF samples after 40 days did not present this shrinkage process, and also after 100 days
 602 the expansion trend slope was higher. This constant increased expansion found in CPF and CPG
 603 samples is due to the presence of expansive compounds in the LFS, associated with the hydration
 604 process of periclase and the formation of brucite as mentioned in the previous CC curing
 605 environment, that overlapped with the lixiviation process. However, now as this sample is subjected
 606 to an accelerated curing environment (submerged in water at 70°C), the periclase hydration process
 607 in the CPF samples is accelerated, reaching the arbitrary limit sooner. In addition, the periclase
 608 hydration process in CPG sample is activated, which makes the CPG sample to differ in its
 609 expansive behavior from the CPC sample, showing an intermediate expansion trend relative to CPC
 610 and CPF samples.

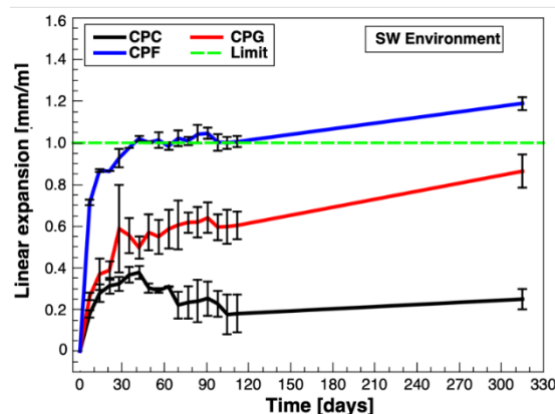
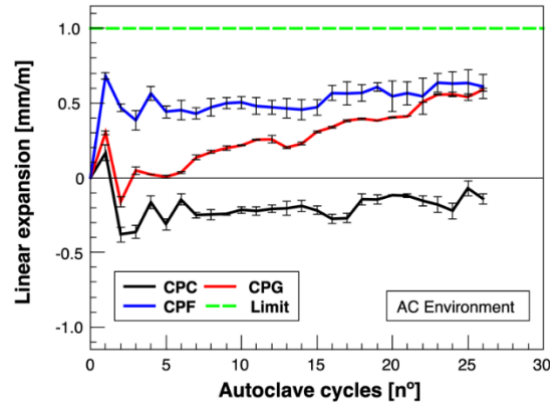


Figure 3-13: Volumetric instability of samples cured in SW environment.

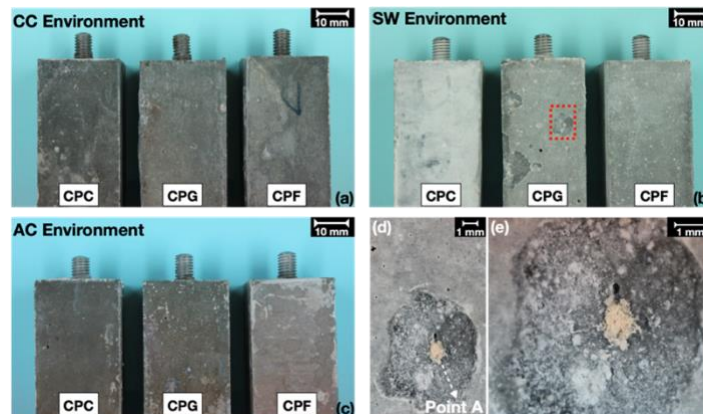
614 Figure 3-14 shows the behavior for the samples CPC, CPG, and CPF at the AC curing environment.
 615 It is observed that all samples show an initial expansion (at different intensities), due to the storage in
 616 a humid curing environment. Then, a slight retraction is observed (also at different intensities), due
 617 to change in the environment to the extreme conditions (from humid chamber to autoclave cycles).
 618 After these changes, a relative tendency towards expansion is manifested in all samples.
 619 CPC sample is the one with the lowest overall expansion which does not exceed the initial retraction
 620 process, reaching a relative value of 0.3 mm/m. In turn, the CPG and CPF samples display similar
 621 overall expansion values close to 0.6 mm/m, but with different evolutions (expansion tendencies
 622 after the initial reactions). This expansion behavior in CPF and CPG samples exceed the initial
 623 retraction, due to the presence of expansive compounds in the slag, associated with the hydration
 624 process of periclase and the formation of brucite, as mentioned before. This initial increase is faster

625 in the CPF sample and more gradual in the case of the CPG sample. The difference in this behavior
 626 can be correlated to the presence of expansive compounds in the slag, as we mentioned in the case of
 627 CC and SW curing environment and the different particle size distribution. However, when it is
 628 subjected to an extreme accelerated curing environment (autoclave cycles at 135 °C and 2.2 bar
 629 pressure), periclase hydration processes are accelerated even more in the CPG samples, so it
 630 manifests more rapidly, achieving similar final values of the maximum controlled expansion for the
 631 CPF sample in the controlled time.
 632



633
 634 **Figure 3-14: Volumetric instability of samples subjected to AC environment.**

635 A visual inspection of the samples tested for volume instability in the different cured conditions it is
 636 shown in Figure 3-15. It can be observed that in the CC environment, (see Figure 3-15(a)) all the
 637 samples did not present any significant changes. This was not the case for the SW environment, as
 638 observed in Figure 3-15(b). The CPC and CPF samples did not present any noticeable changes.
 639 Instead, the CPG sample showed some disintegration of its borders, and the presence of pop-ups in
 640 its surface with a characteristic “orange-yellow” particle at the center, as can be seen in Figure
 641 3-15(d-e). This particle was designated as point A for later analyses.
 642



643
 644 **Figure 3-15: Samples of the different curing environments for volumetric instability test. (a) Cured in wet**
 645 **chamber (CC); (b) Cured submerged in water at 70°C (SW); (c) Subjected to 25 autoclave cycles (AC); (d-e) Pop-**
 646 **up zoom in marked in CPG sample at SW environment.**

647 Figure 3-16 shows the XRD scan of point A between 17° and 50° in 2θ. The XRD results show the
 648 presence of brucite with its characteristic reflections. Magnesite peaks overlapping with calcite also
 649 seem to show up. In contrast, no periclase is detected. The presence of brucite ad magnesite confirms
 650 the advanced hydration state of periclase, and the pop-ups in its surface, a macrostructural
 651 manifestation, that could be related to the hydration of periclase in LFS-G and the associated
 652 expansive process, which were able to produce this type of damage in a rigid matrix. CPF samples
 653 did not show this behavior in the evaluated test time, which could be related to the smaller average

particle size, since a single LFS-F particle produce lesser expansion than LFS-G bigger particles, and not visually damage its surrounding matrix. However, globally the sum of all these lesser expansion produces a higher linear expansion as observed in all the environment tested.

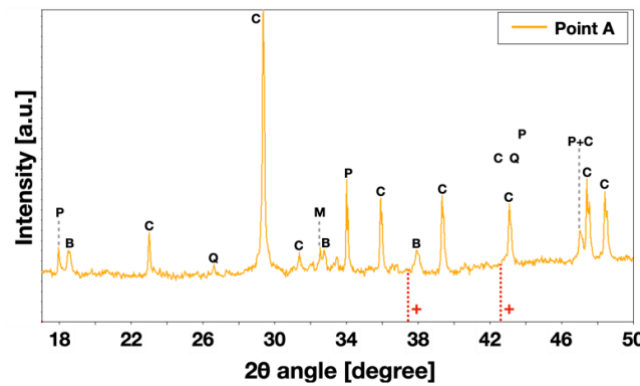


Figure 3-16: Diffractogram of the “orange-yellow dot” at the center of the pop-up for CPG sample cured in SW environment where (P) portlandite; (B) brucite; (C) calcite; (Q) quartz; (M) magnesite; (+) periclase.

4 Conclusions

In the present work, an extensive experimental research was conducted in order to characterize the microstructure and the macrostructural mechanical behavior of LFS in cement-slag systems. Our data and analysis suggest that a partial replacement of Portland cement with LFS could be advantageous from an environmental point of view due to the combined effect of reduced cement usage and the recovery of LFS as a waste from the steel industry.

The results obtained in this work make it possible to correlate the evolution of the microstructural behavior of the cement-LFS system with the physical properties at the macrostructural level. These changes can be attributed to the formation of an amorphous phase "C-S-H gel", portlandite, calcite, and AFm-AFt phases. It has been confirmed that cement hydration reactions govern the hydration process in LFS-cement systems, in addition to a filler effect of the non-reactive phases of LFS. LFS-cement samples show lower mechanical performance mainly due to the cement dilution effect and a dependence to particle size distribution. This observation can be related to a higher SSA and reactivity for LFS-F, which accelerates the hydration reactions and increases the formation of hydration products such as C-S-H gel, and a filler effect that can densify the cementitious matrix. In spite of this, considerable compressive strength values over 55 MPa and 85 MPa were achieved in LFS-cement pastes, opening a possibility as an alternative material for the construction of temporary structures or buildings with a short lifespan.

LFS-cement samples display an increase in volume instability performance compared to the control sample depending on particle size and type of curing environment. The LFS mineralogical composition is a crucial factor in their performance as a cement replacement. Furthermore, it is concluded that special attention must be paid to the evolution of periclase as hydration evolves. As observed in this study, in the absence of free CaO due to weathering/maturity process, free MgO is the main phase associated with the volume instability problems in LFS-cement samples.

Also, the exposed environment needs to be considered for future uses, as it can accelerate the hydration reactions and enhance the expansive behavior. As observed in the CPG sample, SW and AC environments activate LFS-G particles and differentiate its behavior from the control sample, giving rise to expansibility values similar to those of the CPF sample.

5 Acknowledgements

This work was supported by the National Agency for Research and Development (ANID) DOCTORADO EN EL EXTRANJERO, BECAS CHILE/2019 – 72200568. And a special

acknowledgment to Dr. Roberto Lavín Serrano, head of the “Nanotechnology and Cosmic Dust Laboratory” at Universidad Diego Portales, Santiago, Chile, for his advice, contribution and disposition to access the FTIR equipment.

Reference

- [1] M. Schneider, The cement industry on the way to a low-carbon future, *Cem. Concr. Res.* 124 (2019) 105792. doi:10.1016/j.cemconres.2019.105792.
- [2] L. Kriskova, Y. Pontikes, Ö. Cizer, G. Mertens, W. Veulemans, D. Geysen, et al., Effect of mechanical activation on the hydraulic properties of stainless steel slags, *Cem. Concr. Res.* 42 (2012) 778–788. doi:10.1016/j.cemconres.2012.02.016.
- [3] N.A. Madlool, R. Saidur, N.A. Rahim, M. Kamalisarvestani, An overview of energy savings measures for cement industries, *Renew. Sust. Energ. Rev.* 19 (2013) 18–29. doi:10.1016/j.rser.2012.10.046.
- [4] B. Lothenbach, K. Scrivener, R.D. Hooton, Supplementary cementitious materials, *Cem. Concr. Res.* 41 (2011) 1244–1256. doi:10.1016/j.cemconres.2010.12.001.
- [5] M. Thomas, *Supplementary Cementing Materials in Concrete*, 1st ed., CRC Press, Boca Raton, 2013. doi:https://doi.org/10.1201/b14493.
- [6] S. Pauliuk, R.L. Milford, D.B. Müller, J.M. Allwood, The Steel Scrap Age, *Environ. Sci. Technol.* (2013) 1–7. doi:10.1021/es303149z.
- [7] J. Morfeldt, W. Nijs, S. Silveira, The impact of climate targets on future steel production - an analysis based on a global energy system model, *J. Clean. Prod.* 103 (2015) 469–482. doi:10.1016/j.jclepro.2014.04.045.
- [8] World Steel Association, *Steel Statistical Yearbook 2019 Concise version*, 2019. < www.worldsteel.org >
- [9] C. Shi, Steel Slag—Its Production, Processing, Characteristics, and Cementitious Properties, *J. Mater. Civ. Eng.* 16 (2004) 230–236. doi:10.1061/(ASCE)0899-1561(2004)16:3(230).
- [10] Y. Jiang, T.-C. Ling, C. Shi, S.-Y. Pan, Characteristics of steel slags and their use in cement and concrete—A review, *Resour. Conserv. Recycl.* 136 (2018) 187–197. doi:10.1016/j.resconrec.2018.04.023.
- [11] J. Zhao, P. Yan, D. Wang, Research on mineral characteristics of converter steel slag and its comprehensive utilization of internal and external recycle, *J. Clean. Prod.* 156 (2017) 50–61. doi:10.1016/j.jclepro.2017.04.029.
- [12] CEDEX, *Escorias de acería de horno de arco eléctrico, Catálogo de residuos utilizables en construcción, Ficha técnica 2.3*, 2013. < www.cedex.es >
- [13] Á. Rodríguez, S. Gutiérrez-González, I. Santamaría-Vicario, V. Calderón, C. Junco, J. Gadea, Hydration in Mortars Manufactured with Ladle Furnace Slag (LFS) and the Latest Generation of Polymeric Emulsion Admixtures, in: M.M.R. Taha (Ed.), *International Congress on Polymers in Concrete (ICPIC 2018)*, Springer International Publishing, Cham, 2018: pp. 485–490. doi:10.1007/978-3-319-78175-4_62.
- [14] J.M. Montenegro-Cooper, M. Celemín-Matachana, J. Cañizal, J.J. González, Study of the expansive behavior of ladle furnace slag and its mixture with low quality natural soils, *Constr. Build. Mater.* 203 (2019) 201–209. doi:10.1016/j.conbuildmat.2019.01.040.
- [15] J.M. Manso, M. Losañez, J.A. Polanco, J.J. Gonzalez, Ladle Furnace Slag in Construction, *J. Mater. Civ. Eng.* 17 (2005) 513–518. doi:10.1061/(ASCE)0899-1561(2005)17:5(513).
- [16] J.M. Manso, Á. Rodríguez, Á. Aragón, J.J. Gonzalez, The durability of masonry mortars made with ladle furnace slag, *Constr. Build. Mater.* 25 (2011) 3508–3519. doi:10.1016/j.conbuildmat.2011.03.044.
- [17] J. Setién, D. Hernández, J.J. González, Characterization of ladle furnace basic slag for use as a construction material, *Constr. Build. Mater.* 23 (2009) 1788–1794. doi:10.1016/j.conbuildmat.2008.10.003.

- [18] I. Papayianni, E. Anastasiou, Optimization of ladle furnace slag for use as a supplementary cementing material, in: *Measuring, Monitoring and Modeling Concrete Properties*, Springer, Dordrecht, Dordrecht, 2006: pp. 411–417. doi:10.1007/978-1-4020-5104-3_50.
- [19] I. Papayianni, E. Anastasiou, Production of high-strength concrete using high volume of industrial by-products, *Constr. Build. Mater.* 24 (2010) 1412–1417. doi:10.1016/j.conbuildmat.2010.01.016.
- [20] Á. Rodríguez, J.M. Manso, Á. Aragón, J.J. Gonzalez, Strength and workability of masonry mortars manufactured with ladle furnace slag, *Resour. Conserv. Recycl.* 53 (2009) 645–651. doi:10.1016/j.resconrec.2009.04.015.
- [21] A. Rađenović, J. Malina, T. Sofilić, Characterization of Ladle Furnace Slag from Carbon Steel Production as a Potential Adsorbent, *Adv. Mater. Sci. Eng.* 2013 (2013) 1–6. doi:10.1155/2013/198240.
- [22] I.Z. Yildirim, M. Prezzi, Experimental evaluation of EAF ladle steel slag as a geo-fill material: Mineralogical, physical & mechanical properties, *Constr. Build. Mater.* 154 (2017) 23–33. doi:10.1016/j.conbuildmat.2017.07.149.
- [23] H. Yi, G. Xu, H. Cheng, J. Wang, Y. Wan, H. Chen, An Overview of Utilization of Steel Slag, *Procedia Environ. Sci.* 16 (2013) 791–801. doi:10.1016/j.proenv.2012.10.108.
- [24] M. Prieto, M. González, Á. Rodríguez, A. Cobo, The Influence of Replacing Aggregates and Cement by LFS on the Corrosion of Steel Reinforcements, *Appl. Sci.* 9 (2019) 683–14. doi:10.3390/app9040683.
- [25] C. Shi, Characteristics and cementitious properties of ladle slag fines from steel production, *Cem. Concr. Res.* 32 (2002) 459–462.
- [26] W. Posch, H. Presslinger, H. Hiebler, Mineralogical evaluation of ladle slags at voestalpine Stahl GmbH, *Ironmak. Steelmak.* 29 (2002) 308–312. doi:10.1179/030192302225005169.
- [27] M. Tossavainen, F. Engstrom, Q. Yang, N. Menad, M. Lidstrom Larsson, B. Bjorkman, Characteristics of steel slag under different cooling conditions, *Waste Manag.* 27 (2007) 1335–1344. doi:10.1016/j.wasman.2006.08.002.
- [28] I.Z. Yildirim, M. Prezzi, Chemical, Mineralogical, and Morphological Properties of Steel Slag, *Adv. Civ. Eng.* 2011 (2011) 1–13. doi:10.1155/2011/463638.
- [29] C. Shi, J. Qian, High performance cementing materials from industrial slags — a review, *Resour. Conserv. Recycl.* 29 (2000) 195–207. doi:10.1016/S0921-3449(99)00060-9.
- [30] V.Z. Serjun, B. Mirti, A.M.M. Technol, 2013, Evaluation of ladle slag as a potential material for building and civil engineering, *Mater. Technol.* 47 (2013) 543–550.
- [31] I. Papayianni, E. Anastasiou, Effect of granulometry on cementitious properties of ladle furnace slag, *Cem. Concr. Compos.* 34 (2012) 400–407. doi:10.1016/j.cemconcomp.2011.11.015.
- [32] S. Choi, J. Kim, Hydration reactivity of calcium-aluminate-based ladle furnace slag powder according to various cooling conditions, *Cem. Concr. Compos.* 114 (2020) 103734. doi:10.1016/j.cemconcomp.2020.103734.
- [33] J. Zhao, Q. Liu, K. Fang, Optimization of f-MgO/f-CaO phase in ladle furnace slag by air rapidly cooling, *Mater. Lett.* 280 (2020) 128528–9. doi:10.1016/j.matlet.2020.128528.
- [34] D. Adolfsson, R. Robinson, F. Engström, B. Björkman, Influence of mineralogy on the hydraulic properties of ladle slag, *Cem. Concr. Res.* 41 (2011) 865–871. doi:10.1016/j.cemconres.2011.04.003.
- [35] T. Herrero, I.J. Vegas, A. Santamaría, J.T. San-José, M. Skaf, Effect of high-alumina ladle furnace slag as cement substitution in masonry mortars, *Constr. Build. Mater.* 123 (2016) 404–413. doi:10.1016/j.conbuildmat.2016.07.014.
- [36] A. Rodríguez, I. Santamaría-Vicario, V. Calderón, C. Junco, J. García-Cuadrado, Study of the expansion of cement mortars manufactured with Ladle Furnace Slag LFS, *Mater. Constr.* 69 (2019) 183–13. doi:10.3989/mc.2019.06018.

- [37] D. Adolfsson, F. Engström, R. Robinson, B. Björkman, Cementitious Phases in Ladle Slag, *Steel Res. Int.* 82 (2010) 398–403. doi:10.1002/srin.201000176.
- [38] A.S.-D.-G. Vilaplana, V.J. Ferreira, A.M. López-Sabirón, A. Aranda-Usón, C. Lausín-González, C. Berganza-Conde, et al., Utilization of Ladle Furnace slag from a steelwork for laboratory scale production of Portland cement, *Constr. Build. Mater.* 94 (2015) 837–843. doi:10.1016/j.conbuildmat.2015.07.075.
- [39] J.F. Rivera, N. Cristelo, A. Fernández-Jiménez, R.M. de Gutiérrez, Synthesis of alkaline cements based on fly ash and metallurgic slag: Optimisation of the $\text{SiO}_2/\text{Al}_2\text{O}_3$ and $\text{Na}_2\text{O}/\text{SiO}_2$ molar ratios using the response surface methodology, *Constr. Build. Mater.* 213 (2019) 424–433. doi:10.1016/j.conbuildmat.2019.04.097.
- [40] J.M. Montenegro, M. Celemín-Matachana, J. Cañizal, J. Setién, Ladle Furnace Slag in the Construction of Embankments: Expansive Behavior, *J. Mater. Civ. Eng.* 25 (2013) 972–979. doi:10.1061/(ASCE)MT.1943-5533.0000642.
- [41] E.A. Oluwasola, M.R. Hainin, M.M. A Aziz, Characteristics and Utilization of Steel Slag in Road Construction, *J. Teknol.* 70 (2014) 1–8. doi:10.11113/jt.v70.3591.
- [42] V. Ortega-López, J.M. Manso, I.I. Cuesta, J.J. Gonzalez, The long-term accelerated expansion of various ladle-furnace basic slags and their soil-stabilization applications, *Constr. Build. Mater.* 68 (2014) 455–464. doi:10.1016/j.conbuildmat.2014.07.023.
- [43] E.K. Anastasiou, I. Papayianni, M. Papachristoforou, Behavior of self compacting concrete containing ladle furnace slag and steel fiber reinforcement, *Mater. Des.* 59 (2014) 454–460. doi:10.1016/j.matdes.2014.03.030.
- [44] K.K. Sideris, C. Tassos, A. Chatzopoulos, P. Manita, Mechanical characteristics and durability of self compacting concretes produced with ladle furnace slag, *Constr. Build. Mater.* 170 (2018) 660–667. doi:10.1016/j.conbuildmat.2018.03.091.
- [45] Q. Wang, J. Yang, P. Yan, Cementitious properties of super-fine steel slag, *Powder Technol.* 245 (2013) 35–39. doi:10.1016/j.powtec.2013.04.016.
- [46] F. Pietrini, V. Iori, T. Beone, D. Mirabile, M. Zacchini, Effects of a ladle furnace slag added to soil on morpho-physiological and biochemical parameters of *Amaranthus paniculatus* L. plants, *J. Hazard. Mater.* 329 (2017) 339–347. doi:10.1016/j.jhazmat.2017.01.050.
- [47] T.A. Branca, V. Colla, Possible Uses of Steelmaking Slag in Agriculture: An Overview, in: D. Achilias (Ed.), *Material Recycling Trends and Perspectives*, 2012: pp. 1–22. doi:DOI: 10.5772/31804.
- [48] J.M. Manso, V. Ortega-López, J.A. Polanco, J. Setién, The use of ladle furnace slag in soil stabilization, *Constr. Build. Mater.* 40 (2013) 126–134. doi:10.1016/j.conbuildmat.2012.09.079.
- [49] R. Dippenaar, Industrial uses of slag (the use and re-use of iron and steelmaking slags), *Ironmak. Steelmak.* 32 (2013) 35–46. doi:10.1179/174328105X15805.
- [50] S.-Y. Pan, R. Adhikari, Y.-H. Chen, P. Li, P.-C. Chiang, Integrated and innovative steel slag utilization for iron reclamation, green material production and CO_2 fixation via accelerated carbonation, *J. Clean. Prod.* 137 (2016) 617–631. doi:10.1016/j.jclepro.2016.07.112.
- [51] D.M. Proctor, K.A. Fehling, E.C. shay, J.L.W. and, J.J. Green, C. Avent, et al., Physical and Chemical Characteristics of Blast Furnace, Basic Oxygen Furnace, and Electric Arc Furnace Steel Industry Slags, *Environ. Sci. Technol.* 34 (2000) 1576–1582. doi:10.1021/es9906002.
- [52] E.V. Ranfionich, M. Barra, Reactivity and expansion of electric arc furnace slag in their application in construction, *Mater. Constr.* 51 (2001) 137–148. doi:10.3989/mc.2001.v51.i263-264.359.
- [53] E. Adesanya, H. Sreenivasan, A.M. Kantola, V.-V. Telkki, K. Ohenoja, P. Kinnunen, et al., Ladle slag cement - Characterization of hydration and conversion, *Constr. Build. Mater.* 193 (2018) 128–134. doi:10.1016/j.conbuildmat.2018.10.179.

- [54] Y. Wang, P. Suraneni, Experimental methods to determine the feasibility of steel slags as supplementary cementitious materials, *Constr. Build. Mater.* 204 (2019) 458–467. doi:10.1016/j.conbuildmat.2019.01.196.
- [55] R. Baciocchi, G. Costa, E. Di Bartolomeo, A. Poletti, R. Pomi, Carbonation of Stainless Steel Slag as a Process for CO₂ Storage and Slag Valorization, *Waste Biomass Valor.* 1 (2010) 467–477. doi:10.1007/s12649-010-9047-1.
- [56] R.M. Santos, Da Ling, A. Sarvaramini, M. Guo, J. Elsen, F. Larachi, et al., Stabilization of basic oxygen furnace slag by hot-stage carbonation treatment, *Chem. Eng. J.* 203 (2012) 239–250. doi:10.1016/j.cej.2012.06.155.
- [57] E.E. Chang, C.-H. Chen, Y.-H. Chen, S.-Y. Pan, P.-C. Chiang, Performance evaluation for carbonation of steel-making slags in a slurry reactor, *J. Hazard. Mater.* 186 (2011) 558–564. doi:10.1016/j.jhazmat.2010.11.038.
- [58] UNE-EN 197-1, Cement - Part 1: Composition, specifications and conformity criteria for common cements, AENOR, Madrid, 2011.
- [59] UNE 80103, Test methods of cements. Physical analysis. Actual density determination., AENOR, Madrid, 2013.
- [60] UNE-EN 933-1, Tests for geometrical properties of aggregates - Part 1: Determination of particle size distribution - Sieving method, AENOR, Madrid, 2012.
- [61] T. Montaña, Evaluación de escorias de acería para usos potenciales en construcción y obra civil, Master Thesis, Universitat Politècnica de Catalunya-BarcelonaTech, 2019.
- [62] UNE-EN 196-1, Methods of testing cement - Part 1: Determination of strength, AENOR, Madrid, 2018.
- [63] ASTM C642-13, Standard Test Method for Density, Absorption, and Voids in Hardened Concrete, ASTM International, West Conshohocken, PA, 2013.
- [64] ASTM C1038 / C1038M-19, Standard Test Method for Expansion of Hydraulic Cement Mortar Bars Stored in Water, ASTM International, West Conshohocken, PA, 2019. doi:10.1520/C0109_C0109M.
- [65] ASTM C490 / C490M-17, Standard Practice for Use of Apparatus for the Determination of Length Change of Hardened Cement Paste, Mortar, and Concrete, ASTM International, West Conshohocken, PA, 2017.
- [66] G. Le Saoût, V. Kocaba, K. Scrivener, Application of the Rietveld method to the analysis of anhydrous cement, *Cem. Concr. Res.* 41 (2011) 133–148. doi:10.1016/j.cemconres.2010.10.003.
- [67] R.T. Downs, M. Hall-Wallace, The American mineralogist crystal structure database, *Am. Mineral.* 88 (2003) 247–250.
- [68] T.L. Hughes, C.M. Methven, T.G.J. Jones, S.E. Pelham, P. Fletcher, C. Hall, Determining cement composition by Fourier transform infrared spectroscopy, *Adv. Cem. Based Mater.* 2 (1995) 91–104. doi:10.1016/1065-7355(94)00031-X.
- [69] M. Horgnies, J.J. Chen, C. Bouillon, Overview about the use of Fourier Transform Infrared spectroscopy to study cementitious materials, in: *Mc13*, WIT Press, Southampton, UK, 2013: pp. 251–262. doi:10.2495/MC130221.
- [70] L. Kriskova, Y. Pontikes, Ö. Cizer, A. Malfliet, J. Dijkmans, B. Sels, et al., Hydraulic Behavior of Mechanically and Chemically Activated Synthetic Merwinite, *J. Am. Ceram. Soc.* 97 (2014) 3973–3981. doi:10.1111/jace.13221.
- [71] L. Fernández Carrasco, D. Torrens-Martín, L.M. Morales, S. Martínez-Ramírez, Infrared Spectroscopy in the Analysis of Building and Construction Materials, in: T. Theophanides (Ed.), *Infrared Spectroscopy - Materials Science, Engineering and Technology*, InTech, 2012: pp. 369–382. doi:10.5772/36186.
- [72] J. Li, Q. Yu, J. Wei, T. Zhang, Structural characteristics and hydration kinetics of modified steel slag, *Cem. Concr. Res.* 41 (2011) 324–329. doi:10.1016/j.cemconres.2010.11.018.

- [73] C. Kuenzel, F. Zhang, V. Ferrándiz-Mas, C.R. Cheeseman, E.M. Gartner, The mechanism of hydration of MgO-hydromagnesite blends, *Cem. Concr. Res.* 103 (2018) 123–129. doi:10.1016/j.cemconres.2017.10.003.
- [74] K.L. Scrivener, P. Juilland, P.J.M. Monteiro, Advances in understanding hydration of Portland cement, *Cem. Concr. Res.* 78 (2015) 38–56. doi:10.1016/j.cemconres.2015.05.025.
- [75] ASTM C618-19, Standard Specification for Coal Fly Ash and Raw or Calcined Natural Pozzolan for Use in Concrete, ASTM International, West Conshohocken, PA, 2019. doi:10.1520/C0125.
- [76] UNE-EN 450-1, Fly ash for concrete - Part 1: Definition, specifications and conformity criteria, AENOR, Madrid, 2013.

Appendix A

The FTIR characterization of the control CEM sample is described in depth in this appendix.

A.1 FTIR

Figure A-1 shows the FTIR spectrum of the CEM sample, where some characteristic features formed by the overlapping of the C_3S , C_2S , and C_3A absorption peaks are visible, giving rise to a wide absorption band between 800 and 1100 cm^{-1} , and another band over 500 cm^{-1} due to the vibrations of the Si-O and Al-O bonds [1,2]. The presence of calcite with its characteristic absorption band above 1500 cm^{-1} and a group of peaks around 3000 cm^{-1} are also visible. Additionally, the spectrum reveals its characteristic individual peaks at 700, 1800, and 2500 cm^{-1} due to the different normal modes of vibration of the C-O bonds [1,3]. Also, the presence of gypsum yields its characteristic absorption signal arising from the sulfate group around 1620 cm^{-1} , together with two peaks below 700 cm^{-1} [1,3]. Finally, it is worth mentioning the appearance of the peak around 3640 cm^{-1} , which can be attributed to the stretching vibration of the OH group of portlandite [1-3]. This phase should not be present in the anhydrous cement sample but could be formed due to a slight hydration of the sample during storage or when it was subsequently measured.

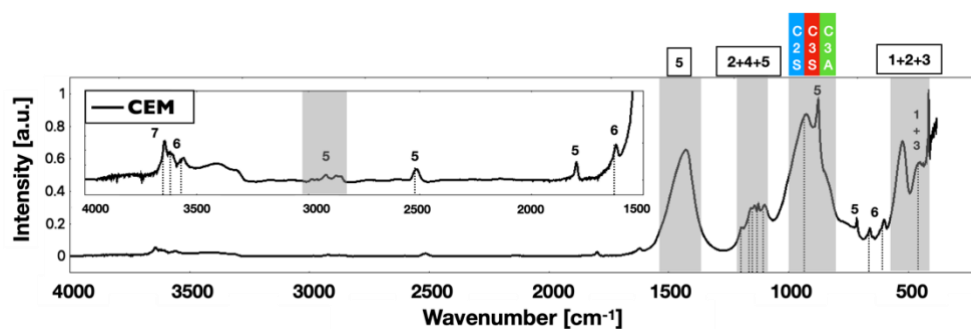


Figure A-1: FTIR spectra of cement, LFS-G and LFS-F raw materials where: (1) C_3S ; (2) β - C_2S ; (3) C_3A ; (4) C_4AF ; (5) calcite; (6) gypsum; (7) portlandite; (8) periclase; (9) C-S-H gel; (10) brucite; (11) wüstite; (12) merwinite; (13) gehlenite; (14) mayenite; (15) γ - C_2S .

Appendix B

The complete microstructural characterization of the control sample (CPC) is described in depth in this appendix.

B.1 SEM

Figure B-1 show SEM/EDX micrographs together with chemical microanalysis of cement paste sample CPC at 60 curing days. Fig shows typical cement paste phases such as (a) a semi-hydrated cement grain with an irregular rounded shape, high content of Ca, Si, and a lighter grayscale tone at the center (anhydrous cement phases C_2S - C_3S) surrounded by a darker grayscale tone halo corresponding to the amorphous hydrated phases C-S-H; (b) AFt/ettringite phase with a needle-like shape and a high content of Ca, Al and S; (c) calcite with bulky irregular column-like formation shape and portlandite as a stack of hexagonal plate shape crystals; and (d) CPC macropore with large amounts of crystal phases such as portlandite and calcite surrounded by a clear amorphous phase C-S-H gel.

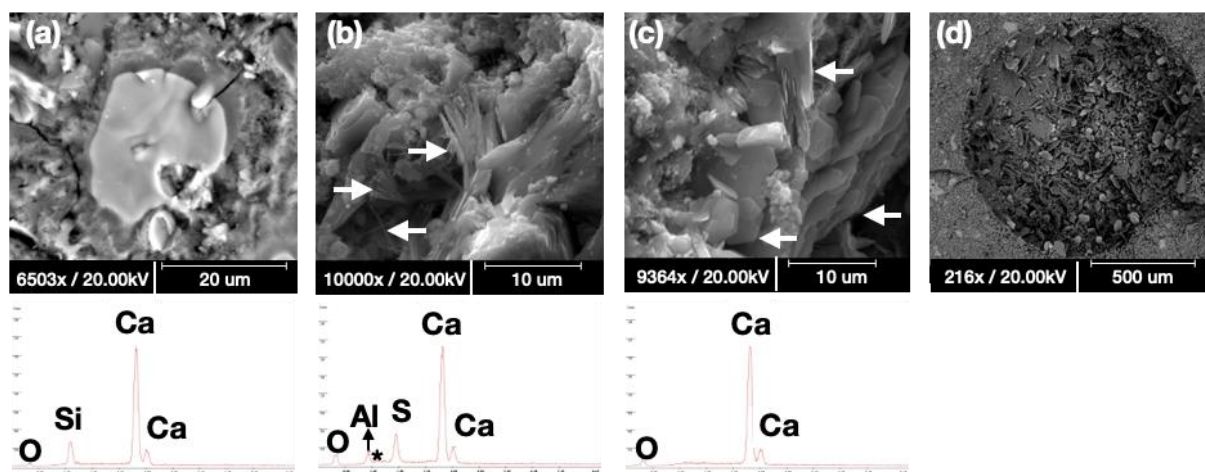


Figure B-1: SEM micrographs and EDX microanalysis of CPC sample at 60 curing days (a) semi hydrated cement grain, (b) AFt phases, (c) portlandite and calcite, (d) CPC macropore.

B.2 XRD

The mineralogical composition of the CPC sample at 7, 28, 60, and 315 days is shown in Figure B-2. First, at 7 curing days the CPC sample shows the characteristic reflections of the crystalline phases presented in ordinary Portland cement pastes due to the hydration process, including portlandite (CH) and ettringite (AFt), together with calcite, the XRD signal of which exhibits a slight intensity increase. A decrease in the main peaks of C_3S , together with the total consumption of C_3A and gypsum phases is also observed. These changes are expected as they correspond to the typical hydration process of cement. At 28 days of curing, there is a slight additional increase in the characteristic peaks of the hydration products, especially those of calcite. AFt is still observed, while the monosulfoaluminate phase (AFm) is not detected. After 60 curing days, no significant changes are observed, with only the appearance of a weak reflection at approximately 11.5° in 2θ that could correspond to the transformation of the low crystalline AFm phase and AFt into the carboaluminate phase. This phase could be formed due to the sizable amount of calcite present in the paste, which favors the formation of this compound. In turn, no significant changes are observed for the calcite reflections. This could be related to the overlapping of the main peak of calcite with those from phases that have been partly consumed (for instance C_2S), which would hide the formation of the

latter. At 315 curing days, a general decrease in the peaks for C_2S and C_3S between the region of 30° - 40° in 2θ is observed, together with an increase of the peaks of portlandite. At this point, a small decrease in the main reflection of calcite is found, which can be attributed to the transformation of AFt/AFm phases to carboaluminate, as suggested by the more intense peak observed for this phase at this particular age. At 315 days, the characteristic XRD peaks of anhydrous CEM phases like C_3S , C_2S and C_4AF are still visible. It should be stressed that a sort of displacement of the baseline in the form of a curvature or hump is visible between 25° to 40° in 2θ . It is well known that this XRD signal is characteristic of the amorphous phase "C-S-H gel" that is formed during the hydration reactions.

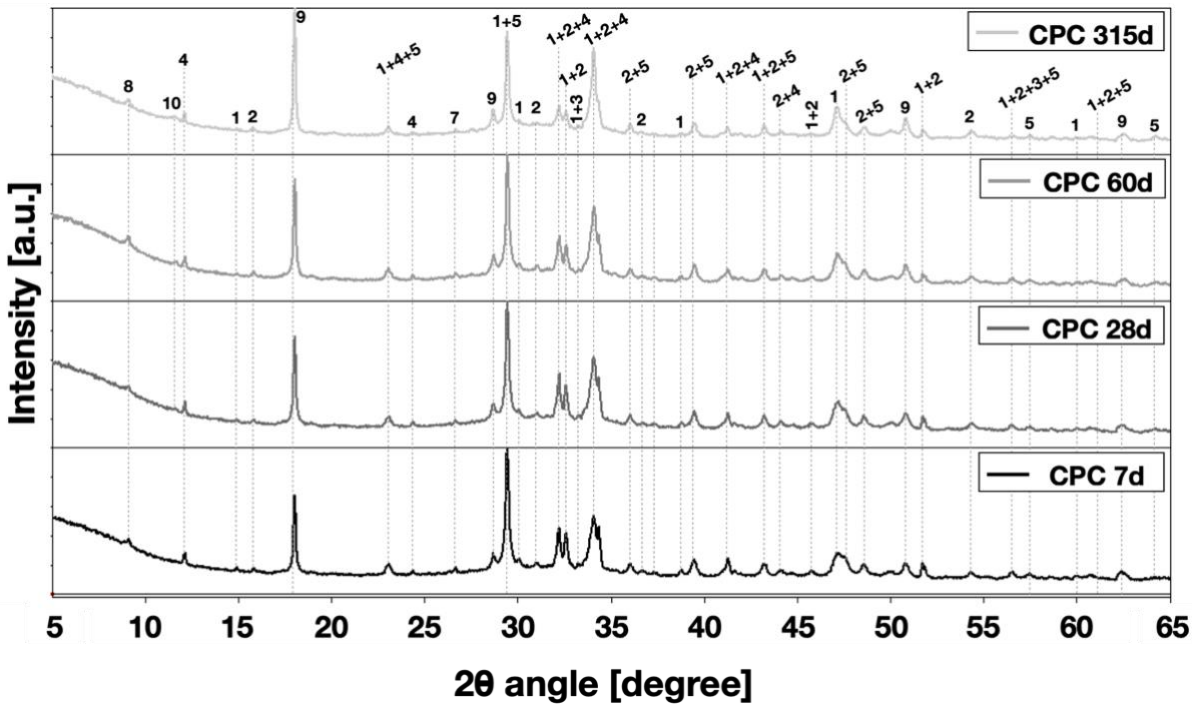


Figure B-2: CPC diffractograms at 7, 28, 60 and 315 curing days where (1) C_3S ; (2) β - C_2S ; (3) C_3A ; (4) C_4AF ; (5) calcite; (7) quartz; (8) AFt; (9) portlandite; (10) carboaluminate.

B.3 FTIR

FTIR transmission spectra of cement pastes sample CPC compared to CEM sample at 7, 28, and 60 curing days are shown in Figure B-3. The evolution of the characteristic compounds of the hydration process already characterized previously with the XRD technique can be observed. It shows the evolution the evolution of CPC sample with some noticeable changes: first the appearance of an amorphous hydrated phase (gel C-S-H) with a wider/broader peak as a hump in the baseline around 3500 - 3400 cm^{-1} and a second well-defined peak at 1630 cm^{-1} , characteristic of the OH group present in the amorphous hydrated phase C-S-H gel due to the hydration of C_3S and C_2S [1-3]. The first peak appears to be age dependent. As time passes, it becomes more evident, so it provides a qualitative way to identify the hydration process of cement and the formation of the C-S-H gel. Also, the second peak is indicative of the formation of other hydrated phases, which can be correlated to the observed displacement of the characteristic peak of gypsum from 1620 cm^{-1} towards 1630 cm^{-1} , after this phase is consumed during the hydration process (note also the disappearance of peaks at 3000 and 700 cm^{-1}). The formation of the AFt-AFm phases is visible through several peaks over 3500 cm^{-1} , 1630 cm^{-1} , and 1100 cm^{-1} [1-3], as can be seen in Fig(b-c). Other characteristic peaks of hydration and formation of C-S-H gel correspond to a shift to the left in the band between 800 - 1000 cm^{-1} (see

Fig(c)), and a shift to the right of the band around 500 cm^{-1} corresponding to the consumption of C_3S and C_3A [4]. A clear increase in the content of portlandite and calcite phases is observed with the increase in the characteristic peaks at 3640 cm^{-1} and the band around 1500 cm^{-1} [1-3], as presented in Fig(a).

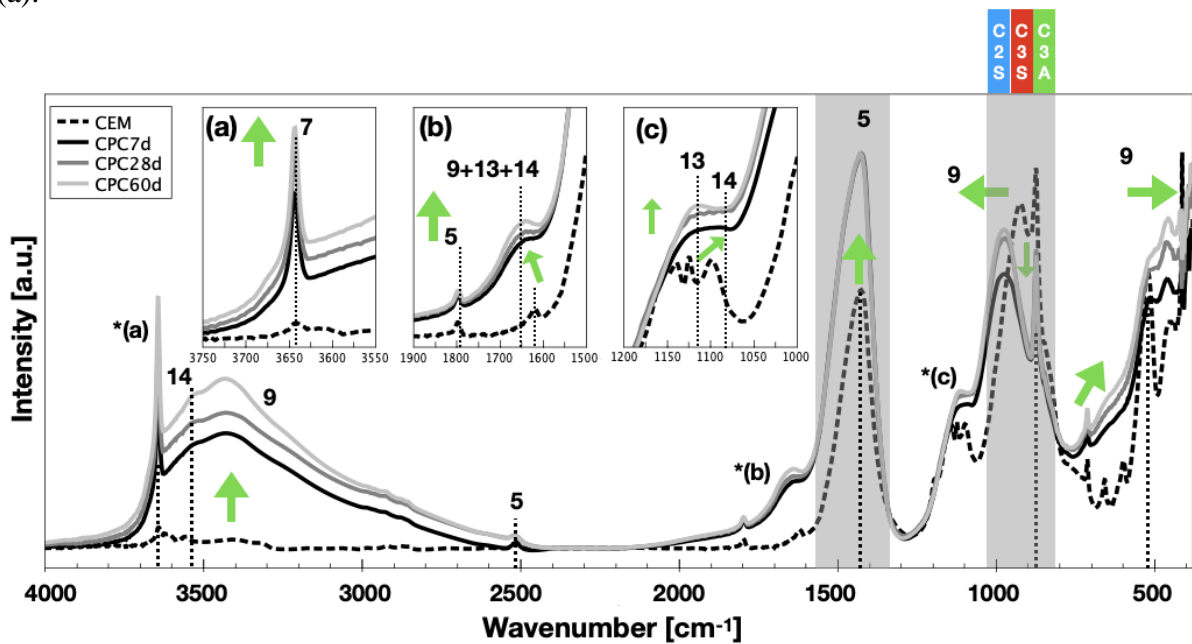


Figure B-3: CPC FTIR spectra at 7, 28 and 60 curing days where: (5) calcite; (7) portlandite; (9) C-S-H gel; (13) AFt; (14) AFm.

Reference

- [1] T.L. Hughes, C.M. Methven, T.G.J. Jones, S.E. Pelham, P. Fletcher, C. Hall, Determining cement composition by Fourier transform infrared spectroscopy, *Adv. Cem. Based Mater.* 2 (1995) 91–104. doi:10.1016/1065-7355(94)00031-X.
- [2] M. Horgnies, J.J. Chen, C. Bouillon, Overview about the use of Fourier Transform Infrared spectroscopy to study cementitious materials, in: *Mc13*, WIT Press, Southampton, UK, 2013: pp. 251–262. doi:10.2495/MC130221.
- [3] L. Fernández Carrasco, D. Torrens-Martín, L.M. Morales, S. Martínez-Ramírez, Infrared Spectroscopy in the Analysis of Building and Construction Materials, in: T. Theophanides (Ed.), *Infrared Spectroscopy - Materials Science, Engineering and Technology*, InTech, 2012: pp. 369–382. doi:10.5772/36186.
- [4] A.H. Delgado, R.M. Paroli, J.J. Beaudoin, Comparison of IR techniques for the characterization of construction cement minerals and hydrated products, *Appl Spectrosc.* 50 (1996) 970-976.